J. Fluid Mech. (2018), *vol.* 835, *pp.* 271–300. © Cambridge University Press 2017
doi:10.1017/jfm.2017.765

Characteristics of the turbulent energy dissipation rate in a cylinder wake

J. G. Chen[1,2,4], Y. Zhou[1,2,†], R. A. Antonia[3] and T. M. Zhou[4]

[1]Institute for Turbulence-Noise-Vibration Interactions and Control, Harbin Institute of Technology (Shenzhen), Shenzhen 518055, China

[2]Digital Engineering Laboratory of Offshore Equipment, Shenzhen 518055, China

[3]School of Engineering, University of Newcastle, NSW 2308, Australia

[4]School of Civil, Environmental and Mining Engineering, The University of Western Australia, 35 Stirling Highway, Crawley, WA 6009, Australia

(Received 6 June 2017; revised 31 August 2017; accepted 19 October 2017; first published online 27 November 2017)

This work aims to improve our understanding of the turbulent energy dissipation rate in the wake of a circular cylinder. Ten of the twelve velocity derivative terms which make up the energy dissipation rate are simultaneously obtained with a probe composed of four X-wires. Measurements are made in the plane of mean shear at $x/d = 10$, 20 and 40, where x is the streamwise distance from the cylinder axis and d is the cylinder diameter, at a Reynolds number of 2.5×10^3 based on d and free-stream velocity. Both statistical and topological features of the velocity derivatives as well as the energy dissipation rate, approximated by a surrogate based on the assumption of homogeneity in the transverse plane, are examined. The spectra of the velocity derivatives indicate that local axisymmetry is first satisfied at higher wavenumbers while the departure at lower wavenumbers is caused by the Kármán vortex street. The spectral method proposed by Djenidi & Antonia (*Exp. Fluids*, vol. 53, 2012, pp. 1005–1013) based on the universality of the dissipation range of the longitudinal velocity spectrum normalized by the Kolmogorov scales also applies in the present flow despite the strong perturbation from the Kármán vortex street and violation of local isotropy at small x/d. The appropriateness of the spectral chart method is consistent with Antonia *et al.*'s (*Phys. Fluids*, vol. 26, 2014, 45105) observation that the two major assumptions in Kolmogorov's first similarity hypothesis, i.e. very large Taylor microscale Reynolds number and local isotropy, can be significantly relaxed. The data also indicate that vorticity spectra are more sensitive, when testing the first similarity hypothesis, than velocity spectra. They also reveal that the velocity derivatives $\partial u/\partial y$ and $\partial v/\partial x$ play an important role in the interaction between large and small scales in the present flow. The phase-averaged data indicate that the energy dissipation is concentrated mostly within the coherent spanwise vortex rollers, in contrast with the model of Hussain (*J. Fluid Mech.*, vol. 173, 1986, pp. 303–356) and Hussain & Hayakawa (*J. Fluid Mech.*, vol. 180, 1987, p. 193), who conjectured that it resides mainly in regions of strong turbulent mixing.

Key words: turbulent flows, vortex streets, wakes

† Email address for correspondence: yuzhou@hit.edu.cn

1. Introduction

The mean turbulent kinetic energy dissipation rate, which plays a major role in small-scale turbulence research (Sreenivasan & Antonia 1997; Vassilicos 2015) is given by

$$\begin{aligned}\overline{\varepsilon} &= \nu\overline{\frac{\partial u_i}{\partial x_j}\left(\frac{\partial u_i}{\partial x_j}+\frac{\partial u_j}{\partial x_i}\right)}\\ &= \nu\Bigg[\underbrace{2\overline{\left(\frac{\partial u}{\partial x}\right)^2}}_{1}+\underbrace{\overline{\left(\frac{\partial v}{\partial x}\right)^2}}_{2}+\underbrace{\overline{\left(\frac{\partial w}{\partial x}\right)^2}}_{3}+\underbrace{\overline{\left(\frac{\partial u}{\partial y}\right)^2}}_{4}+\underbrace{2\overline{\left(\frac{\partial v}{\partial y}\right)^2}}_{5}+\underbrace{\overline{\left(\frac{\partial w}{\partial y}\right)^2}}_{6}\\ &\quad+\underbrace{\overline{\left(\frac{\partial u}{\partial z}\right)^2}}_{7}+\underbrace{\overline{\left(\frac{\partial v}{\partial z}\right)^2}}_{8}+\underbrace{2\overline{\left(\frac{\partial w}{\partial z}\right)^2}}_{9}+\underbrace{2\overline{\frac{\partial u}{\partial y}\frac{\partial v}{\partial x}}}_{10}+\underbrace{2\overline{\frac{\partial u}{\partial z}\frac{\partial w}{\partial x}}}_{11}+\underbrace{2\overline{\frac{\partial v}{\partial z}\frac{\partial w}{\partial y}}}_{12}\Bigg]\end{aligned} \tag{1.1}$$

where an overbar indicates a time-averaged quantity; ν is the kinematic viscosity; u, v and w are the velocity fluctuations in the streamwise (x), lateral (y) and spanwise (z) directions, respectively. The definition of the coordinate system is shown in figure 1(a).

It is a major challenge to measure all the velocity gradient terms in (1.1) with adequate accuracy (see Wallace & Foss 1995; Wallace 2009). As a result, experimental data of $\overline{\varepsilon}$ are usually incomplete in the literature (e.g. Antonia, Anselmet & Chambers 1986; Browne, Antonia & Shah 1987; Saarenrinne & Piirto 2000; Mi & Antonia 2010); a possible exception is the atmospheric surface layer data of Gulitski *et al.* (2007). Consequently, various simplified surrogates are proposed for $\overline{\varepsilon}$ based on different assumptions for the flow. The most widely used assumption is local isotropy, which means that the statistics of the small-scale motions in the flow are invariant with respect to rotations and reflections of the coordinate axis (Pope 2000). The local isotropy assumption, first outlined by Taylor (1935), requires the following equations to be satisfied

$$\overline{\left(\frac{\partial u}{\partial x}\right)^2}=\overline{\left(\frac{\partial v}{\partial y}\right)^2}=\overline{\left(\frac{\partial w}{\partial z}\right)^2}, \tag{1.2}$$

$$2\overline{\left(\frac{\partial u}{\partial x}\right)^2}=\overline{\left(\frac{\partial u}{\partial y}\right)^2}=\overline{\left(\frac{\partial u}{\partial z}\right)^2}=\overline{\left(\frac{\partial v}{\partial x}\right)^2}=\overline{\left(\frac{\partial v}{\partial z}\right)^2}=\overline{\left(\frac{\partial w}{\partial x}\right)^2}=\overline{\left(\frac{\partial w}{\partial y}\right)^2}, \tag{1.3}$$

and

$$\overline{\frac{\partial u}{\partial y}\frac{\partial v}{\partial x}}=\overline{\frac{\partial u}{\partial z}\frac{\partial w}{\partial x}}=\overline{\frac{\partial v}{\partial z}\frac{\partial w}{\partial y}}=-\frac{1}{2}\overline{\left(\frac{\partial u}{\partial x}\right)^2}. \tag{1.4}$$

Using (1.2)–(1.4), the mean energy dissipation rate, namely (1.1), can be reduced to

$$\overline{\varepsilon}_{iso}=15\nu\overline{\left(\frac{\partial u}{\partial x}\right)^2}. \tag{1.5}$$

Because of its great simplicity and the ease with which $\partial u/\partial x$ can be obtained via Taylor's hypothesis, equation (1.5) is widely used in estimating the turbulent energy

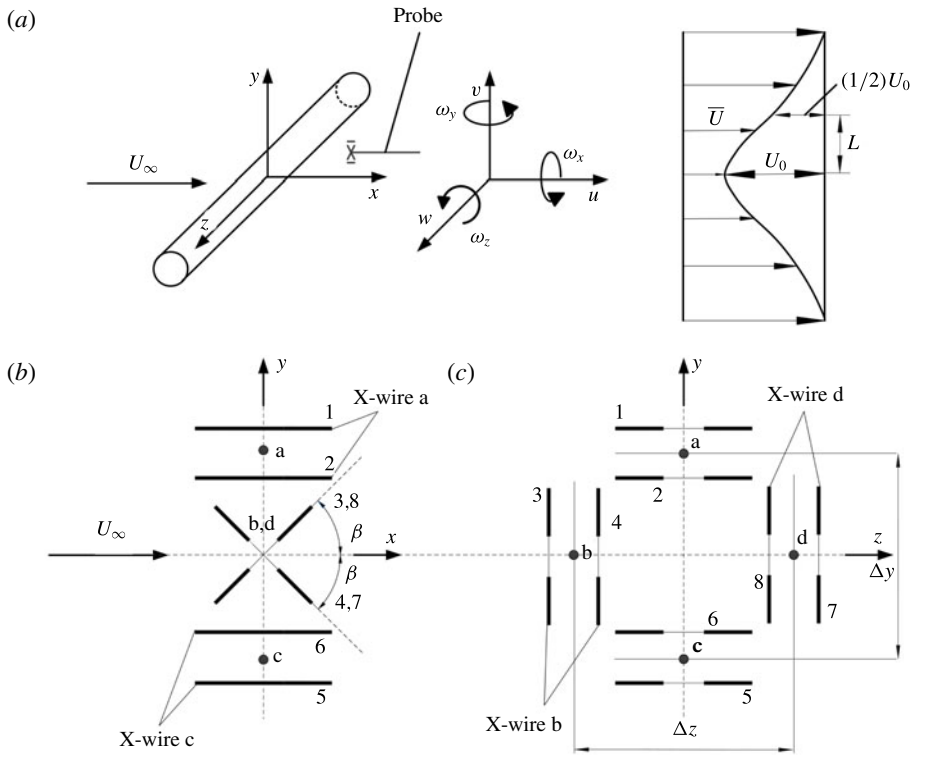

FIGURE 1. (*a*) Experimental arrangement, coordinate system, and definition sketch; (*b*) side view of the vorticity probe; (*c*) front view of the vorticity probe.

dissipation rate in experiments in which the turbulence intensity is not too high (e.g. Browne *et al.* 1987; Antonia, Shah & Browne 1988; Tang *et al.* 2015).

However, many studies have indicated that local isotropy is not an adequate description of the small-scale quantities such as the moment of velocity fluctuation derivatives (e.g. Antonia *et al.* 1986; George & Hussein 1991; Hussein 1994), except at very large Reynolds number (Tang *et al.* 2015). In particular, Browne *et al.* (1987) measured nine mean square terms (1–9 in (1.1)) of $\overline{\varepsilon}$ in a turbulent far wake ($x/d = 420$) and found that $\overline{\varepsilon}$ calculated using isotropy may underestimate the total dissipation rate by 45 %–80 % across the wake. In contrast, a number of previous studies suggested that $\overline{\varepsilon}$ estimated based on the assumption of local axisymmetry (i.e. local invariance with respect to a preferred axis, usually along the streamwise direction) is closer to the true value than that estimated from local isotropy in various turbulent flows, such as round (George & Hussein 1991) and plane (Hussein 1994) jets, the two-dimensional intermediate wake (Mi & Antonia 2010), the far wake (George & Hussein 1991), and the fully developed channel flow (Antonia, Kim & Browne 1991). George & Hussein (1991) outlined the relations between the velocity derivatives that must be satisfied in axisymmetric turbulence, namely,

$$\overline{\left(\frac{\partial u}{\partial y}\right)^2} = \overline{\left(\frac{\partial u}{\partial z}\right)^2}, \quad \overline{\left(\frac{\partial v}{\partial x}\right)^2} = \overline{\left(\frac{\partial w}{\partial x}\right)^2}, \quad \overline{\left(\frac{\partial v}{\partial z}\right)^2} = \overline{\left(\frac{\partial w}{\partial y}\right)^2}, \quad \overline{\left(\frac{\partial v}{\partial y}\right)^2} = \overline{\left(\frac{\partial w}{\partial z}\right)^2} \tag{1.6a–d}$$

$$\overline{\left(\frac{\partial u}{\partial y}\right)^2} = \frac{1}{3}\overline{\left(\frac{\partial u}{\partial x}\right)^2} + \frac{1}{3}\overline{\left(\frac{\partial v}{\partial z}\right)^2} \tag{1.7}$$

$$\overline{\frac{\partial v}{\partial z}\frac{\partial w}{\partial y}} = \frac{1}{6}\overline{\left(\frac{\partial u}{\partial x}\right)^2} - \frac{1}{3}\overline{\left(\frac{\partial v}{\partial z}\right)^2} \tag{1.8}$$

and

$$\overline{\frac{\partial u}{\partial y}\frac{\partial v}{\partial x}} = \overline{\frac{\partial u}{\partial z}\frac{\partial w}{\partial x}} = -\frac{1}{2}\overline{\left(\frac{\partial u}{\partial x}\right)^2}. \tag{1.9}$$

The estimation of the mean energy dissipation rate based on the local axisymmetry assumption is then given by

$$\overline{\varepsilon}_a = \nu\left[\frac{5}{3}\overline{\left(\frac{\partial u}{\partial x}\right)^2} + 2\overline{\left(\frac{\partial u}{\partial z}\right)^2} + 2\overline{\left(\frac{\partial v}{\partial x}\right)^2} + \frac{8}{3}\overline{\left(\frac{\partial v}{\partial z}\right)^2}\right]. \tag{1.10}$$

When the flow is locally homogeneous, i.e. invariant with respect to translation of the coordinate axes, a third simplification of the energy dissipation rate arises (Antonia *et al.* 1991)

$$\overline{\varepsilon}_{hom} = \nu(\overline{\omega_x^2} + \overline{\omega_y^2} + \overline{\omega_z^2}), \tag{1.11}$$

where ω_x, ω_y and ω_z are the vorticity fluctuations in the x, y and z directions, respectively. Antonia *et al.* (1991) found that (1.11) is very well satisfied in a fully developed turbulent channel flow except in the region where the turbulent energy production is maximum (see also Abe, Antonia & Kawamura 2009). In addition, Zhu & Antonia (1996*a*) studied the correlation between enstrophy and energy dissipation rate in a turbulent wake with a probe consisting of four X-wires, of similar design to the probe used in the present study, and assumed homogeneity in the transverse plane (y–z plane) of the wake. Based on this assumption, $\overline{(\partial v/\partial y)(\partial w/\partial z)} \approx \overline{(\partial v/\partial z)(\partial w/\partial y)}$. This has been recently validated by Lefeuvre *et al.* (2014) using direct numerical simulation (DNS) data in the intermediate wake ($x/d = 20$–100) of a square cylinder. The sum of the unmeasured quantities $\overline{(\partial v/\partial y)^2}$ and $\overline{(\partial w/\partial z)^2}$ with the probe can therefore be estimated approximately as $\overline{(\partial u/\partial x)^2} - 2\overline{(\partial v/\partial z)(\partial w/\partial y)}$ using continuity and the approximation $\overline{(\partial v/\partial y)(\partial w/\partial z)} \approx \overline{(\partial v/\partial z)(\partial w/\partial y)}$. The mean energy dissipation rate, assuming homogeneity in the transverse plane, is then given by

$$\begin{aligned}\overline{\varepsilon}_{yz} = \nu\Bigg[&4\overline{\left(\frac{\partial u}{\partial x}\right)^2} + \overline{\left(\frac{\partial u}{\partial y}\right)^2} + \overline{\left(\frac{\partial u}{\partial z}\right)^2} + \overline{\left(\frac{\partial v}{\partial x}\right)^2} + \overline{\left(\frac{\partial v}{\partial z}\right)^2} \\ &+ \overline{\left(\frac{\partial w}{\partial x}\right)^2} + \overline{\left(\frac{\partial w}{\partial y}\right)^2} + 2\overline{\left(\frac{\partial u}{\partial y}\right)\left(\frac{\partial v}{\partial x}\right)} \\ &+ 2\overline{\left(\frac{\partial u}{\partial z}\right)^2\left(\frac{\partial w}{\partial x}\right)^2} - 2\overline{\left(\frac{\partial v}{\partial z}\right)\left(\frac{\partial w}{\partial y}\right)}\Bigg].\end{aligned} \tag{1.12}$$

Using DNS data, Lefeuvre *et al.* (2014) compared the approximations of the mean energy dissipation rate, given by (1.5), (1.10), (1.11) and (1.12), in the

turbulent intermediate wake ($x/d = 20$–100) of a square cylinder, and found that the approximation based on the assumption of local homogeneity in the transverse plane, i.e. equation (1.12), provides the most accurate surrogate of the mean energy dissipation rate. A similar result may be expected for the wake of a circular cylinder even though it may be less isotropic than a square cylinder wake (Thiesset, Danaila & Antonia 2013). This expectation is not unreasonable since $\overline{\varepsilon}_{yz}$ contains nearly all the terms that make up the true energy dissipation rate in (1.1). Unfortunately, the true value of $\overline{\varepsilon}$, as given by (1.1), cannot be obtained with the present probe. Apart from measuring all the velocity derivatives in (1.1), $\overline{\varepsilon}$ can also be estimated indirectly via the energy budget (or the transport equation of the turbulent kinetic energy). For instance, in the nearly homogeneous and isotropic region of grid turbulence, the mean energy dissipation rate can be determined with relatively good accuracy via the turbulent energy budget (e.g. Mohamed & Larue 1990; Zhou & Antonia 2000), *viz.* $\overline{\varepsilon} = -(\overline{U}(\mathrm{d}\overline{q^2}/\mathrm{d}x))/2$, where $\overline{q^2}$ is the turbulent kinetic energy and $\overline{U}$ is the local mean velocity. However, the present flow is far from being homogeneous and isotropic due to the effect of the strongly coherent large-scale vortices and the mean shear. Consequently, the energy budget for the present flow is much more complicated than that for grid turbulence. In particular, the pressure diffusion term is very difficult to measure and is unlikely to be negligible, as has been assumed in the far wake (Tennekes & Lumley 1972; Browne *et al.* 1987). This makes a reliable determination of $\overline{\varepsilon}$ via the energy budget very difficult, if not impossible. To our knowledge, no DNS datasets are available for estimating $\overline{\varepsilon}$ in the present flow. This is also why $\overline{\varepsilon}_{yz}$ has been used as the reference value for the true mean energy dissipation in quite a few studies (e.g. Zhu & Antonia 1996*a*; Yiu *et al.* 2004; Mi & Antonia 2010). In addition, a detailed calibration of the present probe, in the context of measuring the velocity derivatives, was conducted in Antonia, Orlandi & Zhou (2002). In light of the above consideration, we use $\overline{\varepsilon}_{yz}$ as the reference value for $\overline{\varepsilon}$ in this study.

Djenidi & Antonia (2012) reported a simple method for estimating $\overline{\varepsilon}$, which relies on the validity of Kolmogorov's first similarity hypothesis (Kolmogorov 1941), that is, when the Taylor microscale Reynolds number $Re_\lambda (\equiv (\overline{u^2})^{1/2}\lambda/\nu$, where λ is the Taylor microscale) is very large and local isotropy is satisfied, the dissipation range of the velocity spectrum scales uniquely on $\overline{\varepsilon}$ and ν. The spectral chart method greatly simplifies the work of determining $\overline{\varepsilon}$ by avoiding the difficulty associated with measuring spatial velocity derivatives. Antonia, Djenidi & Danaila (2014) pointed out that, when the large-scale term in the transport equation for the second-order structure function $\overline{(\delta u)^2} (\equiv \overline{(u(x+r_1) - u(x))^2}$, where r_1 is the separation distance in the streamwise direction) can be neglected, the collapse of the dissipation range of the longitudinal velocity spectra, normalized by Kolmogorov scales, requires neither of the two major assumptions, *viz.* very large Re_λ and isotropic small-scale structures. This fact essentially highlights the robustness of the Kolmogorov scaling of the dissipative range. The present measurements are made in a turbulent cylinder intermediate wake ($x/d = 10$–40), which is characterized by the gradual streamwise evolution of anisotropic large-scale organized motions, namely the spanwise Kármán vortices and the quasi-streamwise ribs; their features are dominant near the cylinder but gradually impair before disappearing as the distance from the cylinder increases (Zhou *et al.* 2003*b*; Chen *et al.* 2016). It is therefore of great interest and practical importance to assess the spectral chart method, when estimating the mean energy dissipation rate in a flow severely perturbed by large-scale coherent motions. This can also provide some physical insight into the interactions between large- and small-scale motions.

Hussain & Hayakawa (1987) proposed a topological model (shown later in figure 15*a*) for the mechanism of a turbulent plane wake, with the turbulence production occurring mainly along the diverging separatrix and turbulent mixing taking place in the region where the ribs and rollers are in contact with each other. However, this model does not contain information on the spatial distribution of the turbulent energy dissipation. To our knowledge, this information is not available in the literature. The energy dissipation rate is considered to be a fluctuating quantity and, like any other fluctuating quantity, can be affected by large-scale motions (Landau & Lifschitz 1987). Thiesset, Danaila & Antonia (2014) found that the influence of the coherent motion is perceptible even at the smallest scales in the near wake (say $x/d = 10$), and the energy of small scales is enhanced where the coherent strain is maximum. One intuitively expects a relatively strong spatial association of the turbulent energy dissipation with the Kármán vortices. It is therefore fundamentally useful and intriguing to understand how the turbulent energy dissipation is spatially distributed with respect to the Kármán vortices, which prompts us to examine in detail the topology of both the energy dissipation rate and its constituent velocity derivatives.

The paper is organized as follows. Experimental details are given in § 2. Section 3 introduces the phase-averaging technique used to extract the coherent structure from the flow. The statistics of the measured velocity derivatives are examined in § 4. The estimation of using the spectral chart method is discussed in § 5. In § 6, we study the spatial concentrations of the velocity derivatives as well as the energy dissipation rate. We also quantify the contribution from the coherent motions to the mean energy dissipation rate and its components. A more complete topological picture is then proposed, which incorporates the new information for the energy dissipation into Hussain & Hayakawa's (1987) model. Conclusions are given in § 7.

2. Experimental details

A detailed description of the experimental configuration was given in Zhou *et al.* (2003*b*), and here we briefly recall some experimental details that are relevant to the present study. The experiment was conducted in an open-loop low-turbulence wind tunnel with a 2.4 m-long working section of 0.35 m × 0.35 m. A circular cylinder with a diameter $d = 12.7$ mm was used to generate the wake. The free-stream velocity $U_\infty = 3.0$ m s^{-1}. The Reynolds number $Re(\equiv U_\infty d/\nu)$ is 2.5×10^3. A movable probe (figure 1*b*,*c*) consisting of four X-wires was used to measure the velocity fluctuations and their derivatives simultaneously. The separation between the two inclined wires of each cross-wire was approximately 0.6 mm. Two of the X-wires, (b,d), were aligned in the (x, y) plane and separated by $\Delta z = 1.9$ mm; the other two, (a,c), were separated in the (x, z) plane by $\Delta y = 1.9$ mm. Measurements were made at $x/d = 10$, 20 and 40. The cylinder wake has been shown to be statistically symmetric about the centreline (e.g. Zhou *et al.* 2009). As a result, the present measurements were made mainly only on one side of the centreline, i.e. $y/d = -0.2$–2.6, 2.8 and 3.9 for at $x/d = 10$, 20 and 40, respectively. The transverse measurement increment is approximately $0.2d$ for all x/d stations, except for the region near free stream at $x/d = 40$, where the increment was $0.4d$. The output signal from the anemometers was passed through buck and gain circuits and low-pass filtered at a cutoff frequency f_c close to the Kolmogorov frequency $f_k(= \overline{U}_0/(2\pi\eta))$, where $\overline{U}_0$ is the mean streamwise velocity on the centreline of the wake and $\eta \equiv (\nu^3/\overline{\varepsilon})^{1/4}$ is the Kolmogorov length scale. The filtered signal was subsequently sampled at a frequency $f_s = 2f_c$ (3200 Hz at $x/d = 10$ and 20; 2500 Hz at $x/d = 40$) using a 12-bit A/D converter. The record duration was approximately 60 s.

x^*	U_0^*	L^*	U_c^*	Re_λ	$\overline{\varepsilon}$ (m^2 s^{-3})	η (mm)	$\Delta x/\eta$	$\Delta y/\eta$	$\Delta z/\eta$
10	0.22	0.64	0.87	113	4.3	0.17	4.8	11.2	11.2
20	0.18	0.88	0.87	94	1.6	0.21	3.9	9.0	9.0
40	0.14	1.4	0.90	72	0.41	0.30	2.7	6.3	6.3

TABLE 1. Maximum velocity defect, mean velocity half-width, convection velocity, Taylor microscale Reynolds number and spatial resolution of the probe on the wake centreline at different streamwise locations.

The velocity gradient in the y or z direction can be obtained via the ratio of the velocity difference of wires (a,c) or wires (b,d) to Δy or Δz, respectively. The streamwise velocity derivatives are obtained from the temporal derivatives of the corresponding velocity fluctuation using Taylor's hypothesis, i.e. $\Delta u_i/\Delta x \approx \Delta u_i/(-U_c\Delta t)$ where U_c is the convection velocity (table 1) estimated from Zhou & Antonia (1992) and $\Delta t = 1/f_s$.

Table 1 gives the maximum mean velocity defect U_0^*, mean velocity half-width L^*, convection velocity, Taylor microscale Reynolds number and spatial resolution of the probe in terms of the Kolmogorov length scale at the wake centreline of the local x^* position. Hereinafter, the asterisk '*' denotes the normalization by d and/or U_∞. The value of $\overline{\varepsilon}$ is estimated using (1.12). Detailed descriptions of the performance of the probe and the measurement uncertainty of the velocity fluctuations are available in Zhou *et al.* (2003*b*).

It is important to make sure that the spatial resolution of the probe is adequate for the present study of the velocity derivatives and the turbulent energy dissipation rate. Previous measurements indicated that the optimum wire separation of the probe for the velocity derivative measurement is approximately 3–5η (e.g. Antonia, Zhu & Kim 1993; Shafi & Antonia 1997; Zhou, Pearson & Antonia 2001; Zhou *et al.* 2003*b*); a larger wire separation can cause the velocity derivatives to be attenuated, while a smaller wire separation may overestimate the velocity derivatives because of the electronic noise contamination. The present vorticity probe was fabricated, with a great effort, to meet the above criterion of wire separation between the opposite two cross-wires, although the corresponding wire separations $\Delta y/\eta$ and $\Delta z/\eta$ (table 1) are still larger than the optimum value. The velocity derivatives are considered to be underestimated by approximately 18 %–7 % at $x^* = 10$–40, as estimated from error propagations (see § 3 of Zhou *et al.* 2003*b*). Figure 2 shows the comparison between the distribution of $\overline{(\partial u/\partial y)^2}$ in the present measurement at $x^* = 10$ and 40 and those measured by Antonia & Mi (1998). They examined the approach towards self-preservation of the cylinder wake for $x^* = 10$–70 ($Re = 3000$) using two X-wires with a better spatial resolution of approximately 8η at $x^* = 10$ and 5η at $x^* = 40$, which are closer to the optimum spatial resolution of approximately 4η than ours (11η at $x^* = 10$ and 6η at $x^* = 40$, see table 1). The agreement between the two sets of data is actually pretty good, especially at $x^* = 40$. The present measurement appears to be appreciably below that of Antonia & Mi (1998) only near the wake centreline at $x^* = 10$ ($y/L < 0.3$).

Zhu & Antonia (1996*b*) investigated the influence of the probe resolution on the spectra of vorticity measured using a probe with the same geometry used here. They found that the vorticity spectra were attenuated mainly at large wavenumbers (say $k_1\eta > 0.3$, where k_1 is the streamwise wavenumber). Figure 3 shows the spectral

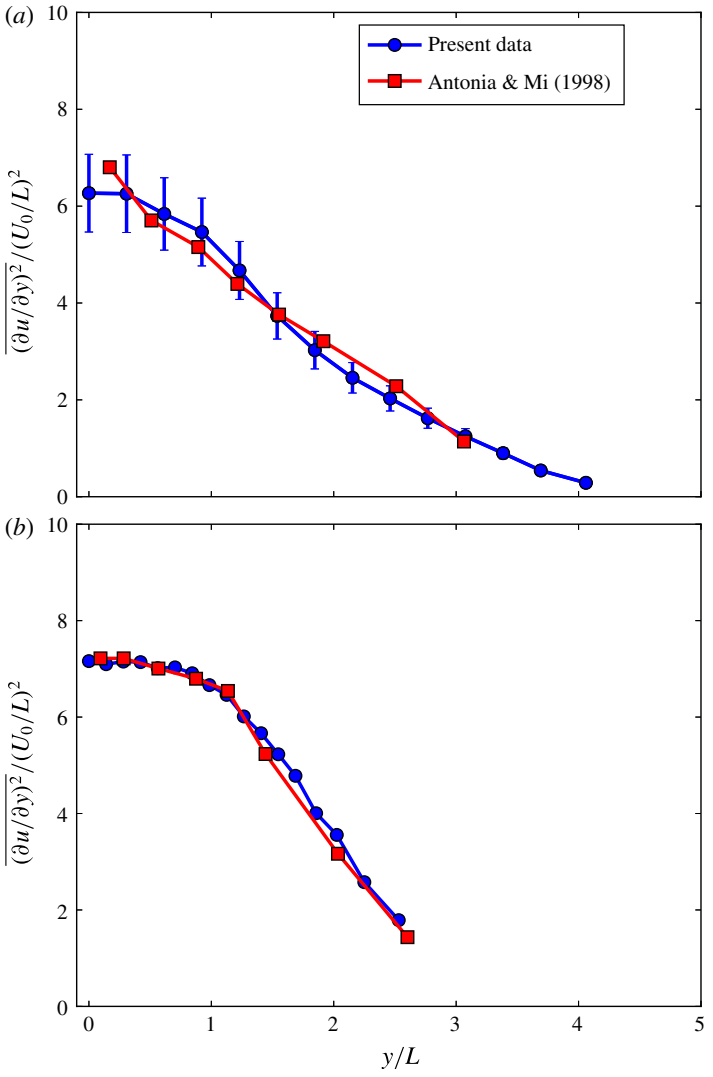

FIGURE 2. (Colour online) Comparison between the present variance of $\partial u/\partial y$ and that in Antonia & Mi (1998) at (*a*) $x^* = 10$ and (*b*) 40. Error bars of the present data at $x^* = 10$ are shown.

density functions of the measured energy dissipation rate (ε_{yz}) on the centreline at $x^* = 10$, 20 and 40 in the form of $k_1\eta F_{\varepsilon_{yz}}(k_1)$ versus $\log(k_1\eta)$. For convenience, $F_{\varepsilon_{yz}}(k_1)$ is normalized so that $\int_0^\infty F_{\varepsilon_{yz}}(k_1)\,\mathrm{d}k_1 = \int_0^\infty \Phi_{\varepsilon_{yz}}(k_1)/\overline{\varepsilon}_{yz}\,\mathrm{d}k_1 = 1$, where $\Phi_{\varepsilon_{yz}}(k_1)$ is the sum of the spectral density of the velocity derivative components on the right-hand side of (1.12). The area under the curve is proportional to the mean energy dissipation rate, and the wavenumber corresponding to the most pronounced peak of the spectrum is related to the most energetic scale. At all x^* positions the scales contributing most to the energy dissipation occur at $k_1\eta \approx 0.16$–0.18, which is consistent with the previous measurements (e.g. Kim & Antonia 1993; She *et al.* 1993; Antonia, Shafi & Zhu 1996; Chen *et al.* 2017). The result suggests that the most energetic

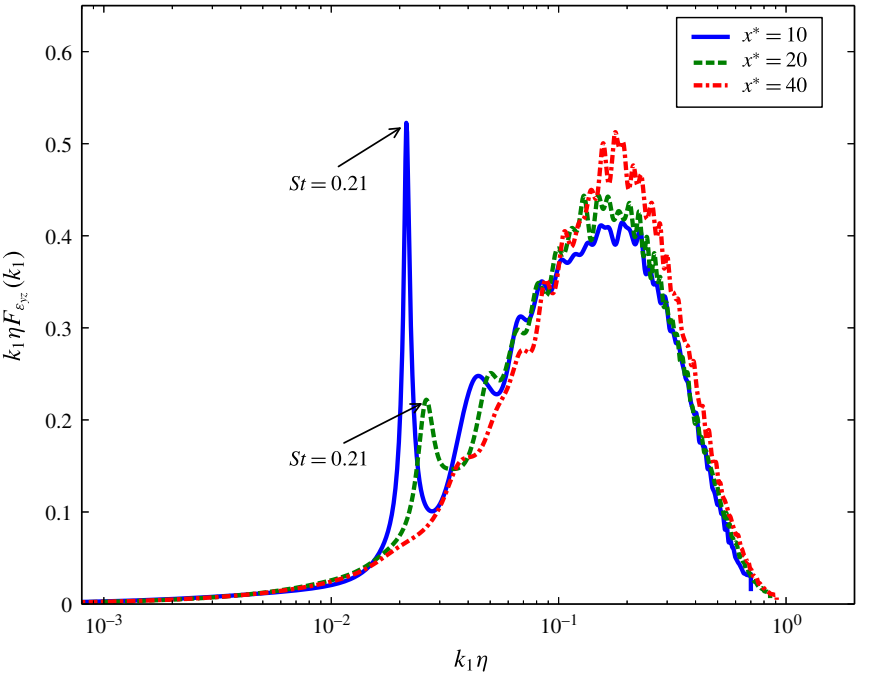

FIGURE 3. (Colour online) Spectral density functions, multiplied by $k_1\eta$, of the turbulent energy dissipation rate ε_{yz} on the wake centreline at $x^* = 10$, 20 and 40.

dissipation process is captured reasonably well in the present measurement. Note that the primary interest of the present study is the spatial distribution of the energy dissipation with respect to the Kármán vortices, whose dimension is comparable to the wake half-width (Hussain & Hayakawa 1987; Chen *et al.* 2016), much larger than the Kolmogorov length scale. Therefore, the measurement attenuation of the very small-scale dissipation will not change the topological result.

3. Phase-averaging technique

3.1. *Phase averaging*

A phase-averaging technique is used to extract the coherent structures from the flow field. The technique is the same as that used in Chen *et al.* (2016, 2017). Briefly, the transverse velocity fluctuation signals v from the probe are filtered using a fourth-order Butterworth filter with the centre frequency set at the vortex shedding frequency $f_{shedding}$, as identified from the most pronounced peak in the v spectrum. A cross-correlation between the measured signal v and the filtered signal v_f is carried out to determine the average phase shift between v_f and the measured v. This shift is then applied to v_f and a new reference signal v_f' is formed. Figure 4 illustrates the v signals at three typical lateral locations at $x^* = 10$ and the corresponding shifted v_f' signals.

Two phases of particular interest are identified on v_f', namely,

$$\text{Phase A: } v_f' = 0 \quad \text{and} \quad \mathrm{d}v_f'/\mathrm{d}t < 0 \tag{3.1}$$

and

$$\text{Phase B: } v_f' = 0 \quad \text{and} \quad \mathrm{d}v_f'/\mathrm{d}t > 0. \tag{3.2}$$

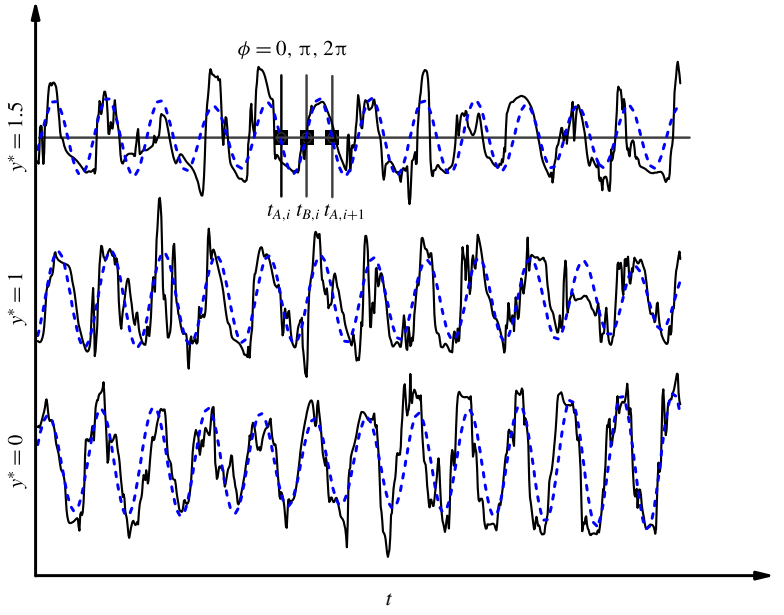

FIGURE 4. (Colour online) Comparison between the measured signal v (the solid line) and the filtered and shifted signal v'_f (the dashed line) at $x^* = 10$.

The two phases correspond to instants $t_{A,i}$ and $t_{B,i}$ (figure 4), respectively. The origin of time is arbitrary. The phase of the measured fluctuation signals is then determined as

$$\phi = \pi \frac{t - t_{A,i}}{t_{B,i} - t_{A,i}}, \quad t_{A,i} < t < t_{B,i} \tag{3.3}$$

and

$$\phi = \pi \frac{t - t_{B,i}}{t_{A,i+1} - t_{B,i}} + \pi, \quad t_{B,i} < t < t_{A,i+1}. \tag{3.4}$$

The interval between phases A and B is made equal to $0.5T_s = 0.5/f_s$ by compressing or stretching and is further divided into 10 equal intervals. Phase averaging was then applied to the measured rather than the filtered signals. The phase average of an instantaneous quantity Γ is given by $\langle \Gamma \rangle_p = (1/N) \sum_{i=1}^{N} \Gamma_{p,i}$, where p represents the phase, and N is the number of detections which are approximately 1800, 1700, and 400 at $x^* = 10$, 20 and 40, respectively.

Based on the triple decomposition (Hussain 1983), Γ may be viewed as the sum of the time-averaged component $\overline{\Gamma}$, and the fluctuating component β, which can be further decomposed into a coherent fluctuation $\widetilde{\beta}$ and a remainder β_r, namely

$$\beta = \widetilde{\beta} + \beta_r. \tag{3.5}$$

The coherent component $\widetilde{\beta} \equiv \langle \beta \rangle$ reflects the effect from the large-scale coherent motions, while β_r is associated with the remaining smaller-scale motions. After multiplying (3.5) with $\gamma = \widetilde{\gamma} + \gamma_r$, we obtain

$$\beta\gamma = \widetilde{\beta}\widetilde{\gamma} + \widetilde{\beta}\gamma_r + \widetilde{\gamma}\beta_r + \beta_r\gamma_r. \tag{3.6}$$

By phase averaging (3.6) and assuming a zero correlation between coherent and remainder fluctuations, i.e. $\langle\widetilde{\beta}\gamma_r\rangle = 0$ and $\langle\widetilde{\gamma}\beta_r\rangle = 0$, we obtain

$$\langle\beta\gamma\rangle = \widetilde{\beta}\widetilde{\gamma} + \langle\beta_r\gamma_r\rangle, \tag{3.7}$$

where β and γ represent velocity fluctuation derivatives $\partial u_i/\partial x_j$, in which u_i stands for u, v, or w, while x_j stands for x, y, or z.

3.2. *Structural averaging*

Once the coherent components are extracted from the examined quantities, the averaged coherent contribution to the product of fluctuating components within one period can be given in terms of the structural average. The conditionally averaged structure begins at n_1 samples (corresponding to $\phi = -\pi$) before $\phi = 0$ and ends at n_2 samples (corresponding to $\phi = \pi$) after $\phi = 0$. The structural average, denoted by a double overbar, is defined by

$$\overline{\overline{\widetilde{\beta}\widetilde{\gamma}}} = \frac{1}{n_1 + n_2 + 1}\sum_{-n_1}^{n_2}\widetilde{\beta}\widetilde{\gamma}. \tag{3.8}$$

4. Mean square velocity derivatives

Ten of twelve terms in (1.1), except terms 5 and 9, can be captured simultaneously with the multiwire probe, which are examined in this section both in the physical and the spectral domains.

Figure 5 shows the lateral distribution of the ten terms, including seven mean square terms and three correlation terms at $x^* = 10$, 20 and 40. For locally isotropic flow, the distributions of the mean square terms and the correlation terms are expected to collapse onto the curves $2\overline{(\partial u/\partial x)^2}$ and $-\overline{(\partial u/\partial x)^2}$ (also shown in figure 5), respectively, as indicated by (1.2) to (1.4). The distributions of the velocity derivative variances show considerable scatter at $x^* = 10$ and 20 (figure 5*a*,*b*), which essentially reflects the effect of the strong anisotropic large-scale vortices, including the spanwise Kármán vortices and the streamwise rib structures, at these positions (e.g. Zhou *et al.* 2003*b*; Chen *et al.* 2016). At $x^* = 40$ (figure 5*c*), where the coherent structures become quite weak, most of the variances collapse together reasonably, except for $\overline{(\partial v/\partial z)^2}$ and $\overline{(\partial w/\partial y)^2}$, which exhibit a nearly equal departure from isotropy. Although $2\overline{(\partial v/\partial y)^2}$ and $2\overline{(\partial w/\partial z)^2}$ in (1.1) have not been measured, the earlier measurements of Mi & Antonia (2010) indicated that these two terms also deviate nearly equally from the expected isotropic distribution $2\overline{(\partial u/\partial x)^2}$ at $x^* = 40$. All the correlation terms are much smaller than the isotropic distribution $-\overline{(\partial u/\partial x)^2}$, even at $x^* = 40$. This departure is expected to diminish downstream as the coherent motions, i.e. the Kármán vortices and ribs, which are predominantly responsible for the anisotropy, vanish gradually. It should be pointed out that the velocity derivative variances would not collapse completely even in the self-preserving far wake, as shown by Browne *et al.* (1987), who measured at $x^* = 420$ nine components of the energy dissipation rate. This by no means implies the persistence of the Kármán vortices and ribs; rather, the anisotropic coherent motions generated due to the shear layer instability in the far wake (e.g. Zhou & Antonia 1995) may be responsible for the observation. On the other hand, the near equalities of $\overline{(\partial v/\partial z)^2}$ and $\overline{(\partial w/\partial y)^2}$ in figure 5(*b*,*c*) and of $2\overline{(\partial v/\partial y)^2}$ and $2\overline{(\partial w/\partial z)^2}$ in Mi & Antonia (2010) comply with the local axisymmetry equations (1.6*c*,*d*), and suggest that local axisymmetry seems to be a more appropriate assumption than local isotropy.

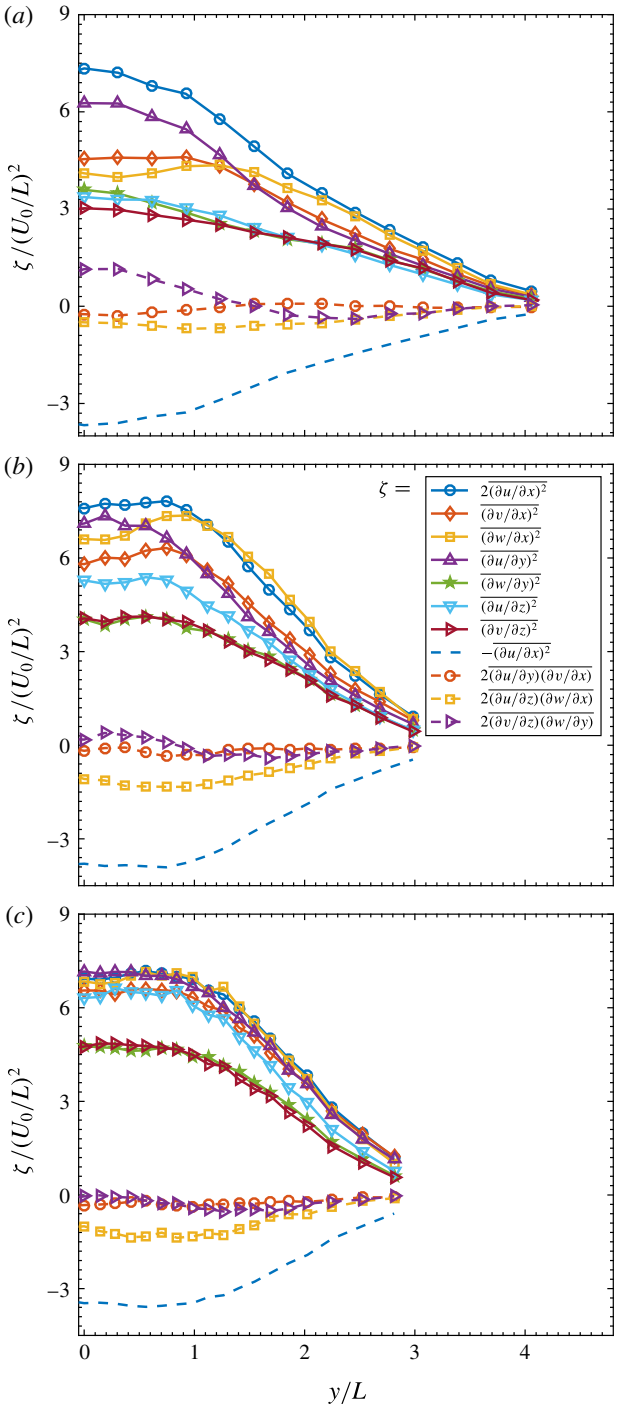

FIGURE 5. (Colour online) Lateral distribution of the constituent velocity derivative variances of the mean energy dissipation rate at (*a*) $x^* = 10$, (*b*) 20, (*c*) 40. ζ represents the velocity derivative terms.

In order to quantify the extent to which both local isotropy and local axisymmetry hold, we have calculated the ratios of the left and right sides of (1.2)–(1.4) (local isotropy) and (1.6)–(1.9) (local axisymmetry). For local isotropy, the ratios are defined by K_i, namely

$$K_1 = \frac{\overline{2(\partial u/\partial x)^2}}{\overline{(\partial v/\partial x)^2}}, \quad K_2 = \frac{\overline{2(\partial u/\partial x)^2}}{\overline{(\partial w/\partial x)^2}}, \quad K_3 = \frac{\overline{2(\partial u/\partial x)^2}}{\overline{(\partial u/\partial y)^2}}, \tag{4.1a–c}$$

$$K_4 = \frac{\overline{2(\partial u/\partial x)^2}}{\overline{(\partial u/\partial z)^2}}, \quad K_5 = \frac{\overline{2(\partial u/\partial x)^2}}{\overline{(\partial w/\partial y)^2}}, \quad K_6 = \frac{\overline{2(\partial u/\partial x)^2}}{\overline{(\partial v/\partial z)^2}}, \tag{4.1d–f}$$

$$K_7 = \frac{\overline{(\partial u/\partial y)(\partial v/\partial x)}}{-1/2\overline{(\partial u/\partial x)^2}}, \quad K_8 = \frac{\overline{(\partial u/\partial z)(\partial w/\partial x)}}{-1/2\overline{(\partial u/\partial x)^2}}, \quad K_9 = \frac{\overline{(\partial v/\partial z)(\partial w/\partial y)}}{-1/2\overline{(\partial u/\partial x)^2}}. \tag{4.1g–i}$$

All these ratios should be unity. For local axisymmetry, the ratios are defined by R_i, namely

$$R_1 = \frac{\overline{(\partial u/\partial y)^2}}{\overline{(\partial u/\partial z)^2}}, \quad R_2 = \frac{\overline{(\partial v/\partial x)^2}}{\overline{(\partial w/\partial x)^2}}, \quad R_3 = \frac{\overline{(\partial v/\partial z)^2}}{\overline{(\partial w/\partial y)^2}}, \tag{4.2a–c}$$

$$R_4 = \frac{\overline{(\partial v/\partial z)(\partial w/\partial y)}}{1/6\overline{(\partial u/\partial x)^2} - 1/3\overline{(\partial v/\partial z)^2}}, \tag{4.2d}$$

$$R_5 = \frac{\overline{(\partial u/\partial y)(\partial v/\partial x)}}{-1/2\overline{(\partial u/\partial x)^2}}, \quad R_6 = \frac{\overline{(\partial u/\partial z)(\partial w/\partial x)}}{-1/2\overline{(\partial u/\partial x)^2}}. \tag{4.2e,f}$$

All these ratios should be unity. Figure 6 contains the distributions of K_i and R_i across the wake at the three x^* positions. As shown in figure 6(*a–c*), as x^* increases, K_1 to K_4 approach 1, while K_7 to K_9, which are associated with the velocity correlation terms, are quite close to zero because of the small magnitude of the correlation terms compared with that of $-(\overline{(\partial u/\partial x)^2})/2$ (figure 5*a–c*). The ratios associated with $\overline{(\partial w/\partial y)^2}$ and $\overline{(\partial v/\partial z)^2}$, i.e. K_5 and K_6, similarly depart from unity, although the departure decreases from $x^* = 10$ to $x^* = 40$. It is noted that K_1 to K_6, which are associated with the mean square terms, are generally larger than 1, indicating that the mean energy dissipation rate based on local isotropy can be overestimated in the present flow, especially at $x^* = 10$ and 20, which is confirmed later in figure 9 in § 5 and is also observed by Mi & Antonia (2010) and Lefeuvre *et al.* (2014). On the other hand, as x^* increases, the ratios R_1 to R_3 associated with the mean square terms gradually approach 1, while R_4 to R_6 associated with the correlation terms behave similarly to K_7 to K_9, that is, they are nearly zero (figure 6*d–f*). Figure 6 indicates that the extent to which both local isotropy and local axisymmetry apply improves downstream for the mean square velocity derivative terms; departures are mainly associated with the velocity derivative correlation terms. Consistent with figure 5, the nearly equal deviation from unity of K_5 and K_6 even at $x^* = 40$ (figure 6*c*), which is consistent with R_3 being close to unity (figure 6*f*), suggests that the local axisymmetry should be a better description than local isotropy for the velocity derivative variances in the present flow.

It should be recognized that K_i and R_i provide some qualification of the extent to which local isotropy and local axisymmetry hold. It is also of interest to assess

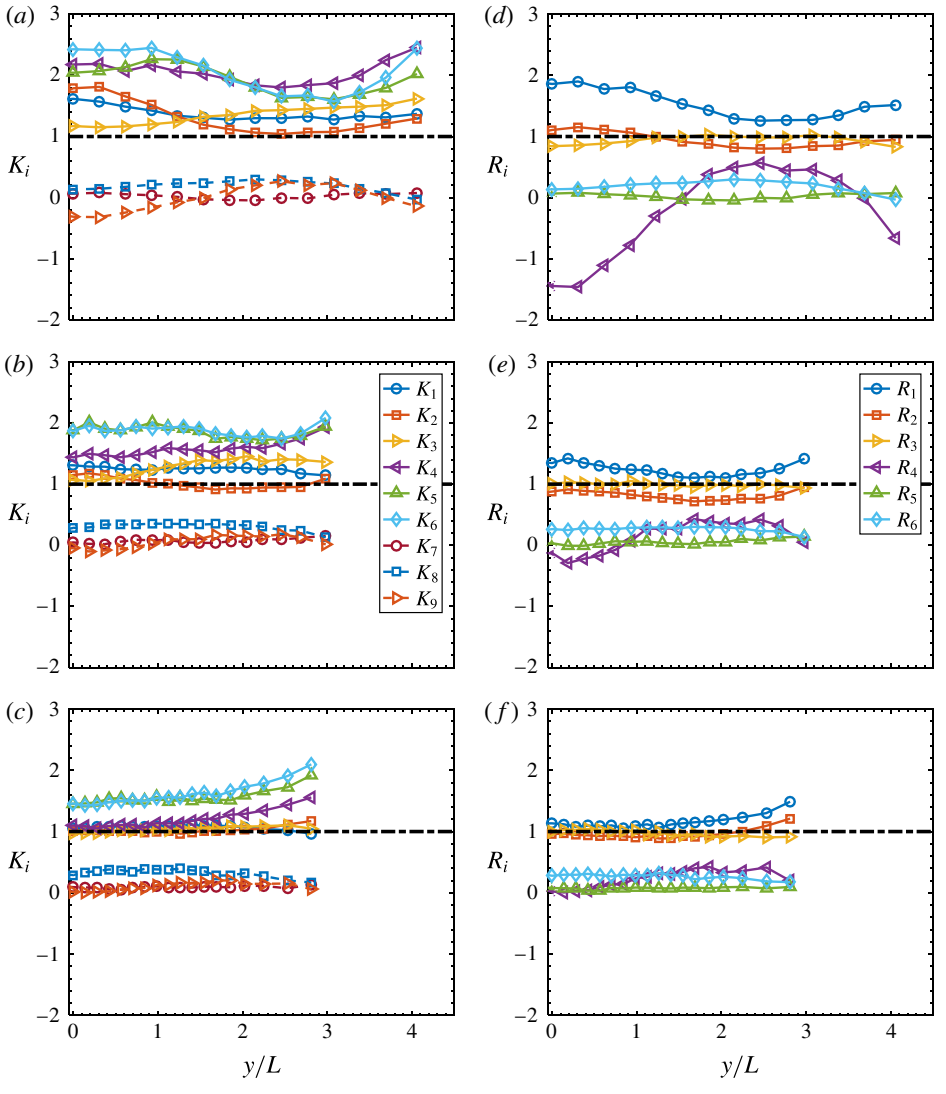

FIGURE 6. (Colour online) Lateral distributions of ratios K_i (4.1*a–i*) and R_i (4.2*a–f*) at (*a*,*d*) $x^* = 10$, (*b*,*e*) 20, (*c*,*f*) 40. The dash-dotted line in each figure corresponds to unity, which is the locally isotropic value for K_i in (*a–c*) and locally axisymmetric value for R_i in (*d–f*).

these assumptions in the spectral space in terms of different flow scales. Figure 7 shows the spectra of the seven measured velocity derivatives at the wake centreline. For convenience of comparing spectra of different velocity derivatives, the spectra are normalized to a unity integral with the variance of the corresponding velocity derivative, i.e. $\int_0^\infty F_{\partial u_i/\partial x_j}(k_1)\,\mathrm{d}k_1 = \int_0^\infty E_{\partial u_i/\partial x_j}(k_1)/\overline{(\partial u_i/\partial x_j)^2}\,\mathrm{d}k_1 = 1$, where $E(k_1)_{\partial u_1/\partial x_j}$, defined such that $\int_0^\infty E_{\partial u_i/\partial x_j}(k_1)\,\mathrm{d}k_1 = \overline{(\partial u_i/\partial x_j)^2}$, is the power spectral density function of $\partial u_i/\partial x_j$. Similar to the spectra of the energy dissipation rate in figure 2, the spectra in figure 7 are presented in the form of $k_1\eta F_{\partial u_i/\partial x_j}$ versus $k_1\eta$ so that the area under the curve is proportional to the variance of the corresponding velocity derivative.

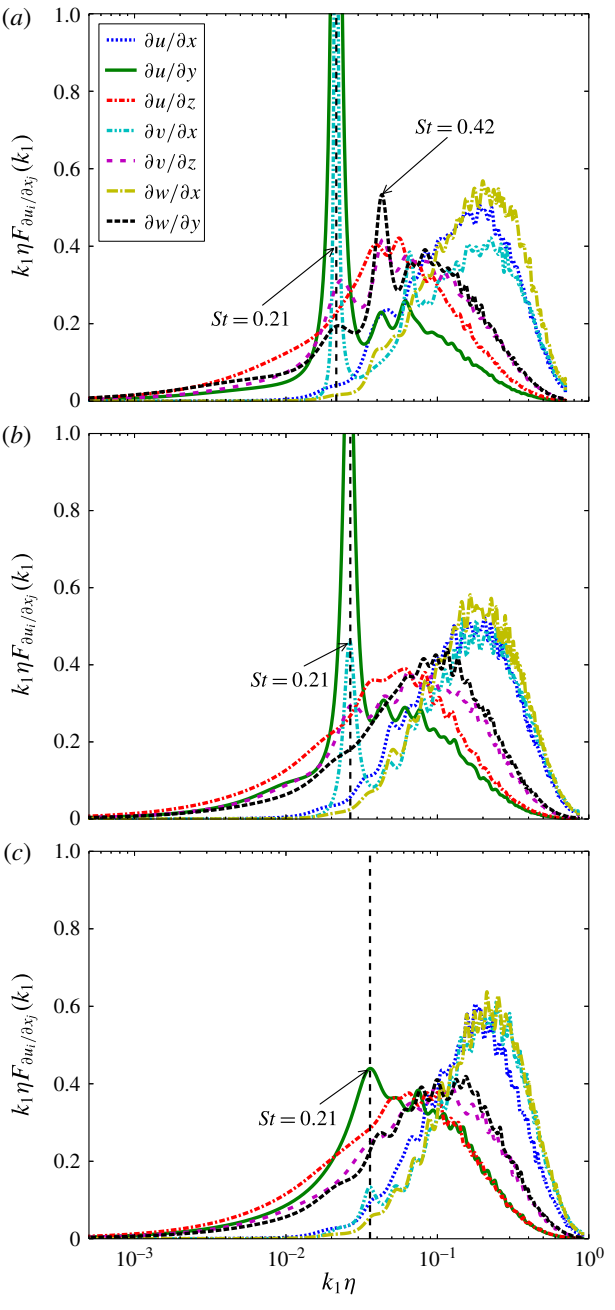

FIGURE 7. (Colour online) Spectral density functions, multiplied by $k_1\eta$, of measured velocity derivatives on the wake centreline at $x^* = 10$, 20 and 40. The vertical dashed line in each figure denotes the wavenumber corresponding to the vortex shedding frequency.

Several observations can be made from figure 7. Firstly, the Kármán vortices have a profound influence on $\partial u/\partial y$ and $\partial v/\partial x$, compared with the other derivatives. The spectra of both $\partial u/\partial y$ and $\partial v/\partial x$ at $x^* = 10$ (figure 7*a*) display a pronounced peak

at the wavenumber corresponding to $St = 0.21$, which is significantly bigger than that in other spectra at the same wavenumber. The pronounced peak in $F_{\partial u/\partial y}$ and $F_{\partial v/\partial x}$ at $St = 0.21$ is obviously a footprint of the spanwise vorticity $\omega_z (= \partial v/\partial x - \partial u/\partial y)$, the most organized vorticity component associated with the Kármán vortices in this flow. At $x^* = 20$ (figure 7*b*), the pronounced peak in $F_{\partial u/\partial y}$ or $F_{\partial v/\partial x}$ at $St = 0.21$ contracts but is still much more evident than that in the other spectra. Even at $x^* = 40$, where the Kármán vortices are quite weak, the peak at $St = 0.21$ in $F_{\partial u/\partial y}$ remains prominent, although the peak in $F_{\partial v/\partial x}$ is just discernible. Note that a peak occurs at the wavenumber corresponding to $St = 0.42$ in the spectrum of $\partial w/\partial y$ at $x^* = 10$ (figure 7*a*), but disappears at $x^* = 20$ and 40. This peak is likely caused by the positive and negative spanwise velocity induced by the rib structures, which are strong and organized even near the wake centreline at $x^* = 10$ but become weak and disordered downstream (Huang, Zhou & Zhou 2006; Djenidi & Antonia 2009; Chen *et al.* 2016).

Secondly, the assumption of local axisymmetry does not necessarily require a collapse in the spectra of the corresponding velocity derivatives on either side of (1.6*a–d*). However, it is interesting to see that, as x^* increases from 10 to 40, the high-wavenumber parts of the spectra gradually collapse into three groups, i.e. $\partial u/\partial y$ and $\partial u/\partial z$, $\partial v/\partial x$ and $\partial w/\partial x$ as well as $\partial w/\partial y$ and $\partial v/\partial z$, which correspond to the local axisymmetry assumption, namely (1.6*a–c*). In contrast, the agreement between the low-wavenumber parts of the corresponding spectra is not so clear because of the effect of the Kármán vortices ($St = 0.21$), especially at $x^* = 10$ and 20. Interestingly, as the pronounced peak in $F_{\partial u/\partial y}$ and $F_{\partial v/\partial x}$ at $St = 0.21$ gradually retreats from $x^* = 10$ to 40, the high-wavenumber behaviours of $F_{\partial u/\partial y}$ and $F_{\partial v/\partial x}$ evolve towards those of $F_{\partial u/\partial z}$ and $F_{\partial w/\partial x}$, respectively, and collapse at $x^* = 40$. The behaviours at the low and the high wavenumbers of $F_{\partial u/\partial y}$ and $F_{\partial v/\partial x}$ suggest that local axisymmetry is first satisfied in the high-wavenumber range, while the departure in the low-wavenumber range is caused by the Kármán-vortex-related motions. It is reasonable to expect that, as the coherent motions weaken further downstream, the agreement between the spectra of the corresponding velocity derivatives should improve in the low-wavenumber range, and local axisymmetry should be better satisfied, as confirmed by Mi & Antonia (2010) with the data of Browne *et al.* (1987) in the self-preserving far wake.

5. Estimation of $\overline{\varepsilon}$ via the spectral chart method

Based on the universality of the dissipative range of the Kolmogorov-normalized longitudinal velocity spectrum, Djenidi & Antonia (2012) proposed a spectral chart method to estimate the mean energy dissipation rate in various flows where Kolmogorov's first similarity hypothesis applies. Specifically, the basic procedure is to use 'guessed' values of the energy dissipation rate to 'un-normalize' a reference universal spectrum iteratively until it collapses onto the measured velocity spectrum over the lower-wavenumber portion of the dissipative range. The focus of this section is to evaluate the spectral chart method to see if it can approximate $\overline{\varepsilon}_{yz}$ in the present flow, notwithstanding the perturbation from the large-scale motions.

Kolmogorov's first similarity hypothesis, which was enunciated in his well-known paper (Kolmogorov 1941), essentially postulates that the statistics of the small-scale motions (in both the dissipative and inertial ranges) are solely determined by $\overline{\varepsilon}$ and ν, provided that the Reynolds number is very large and the small scales are isotropic. One implication of this hypothesis is that the dissipation range of the one-dimensional velocity spectrum, normalized by Kolmogorov scales, will collapse onto a universal function of $k^{\ddagger}$, where '‡' denotes normalization by Kolmogorov

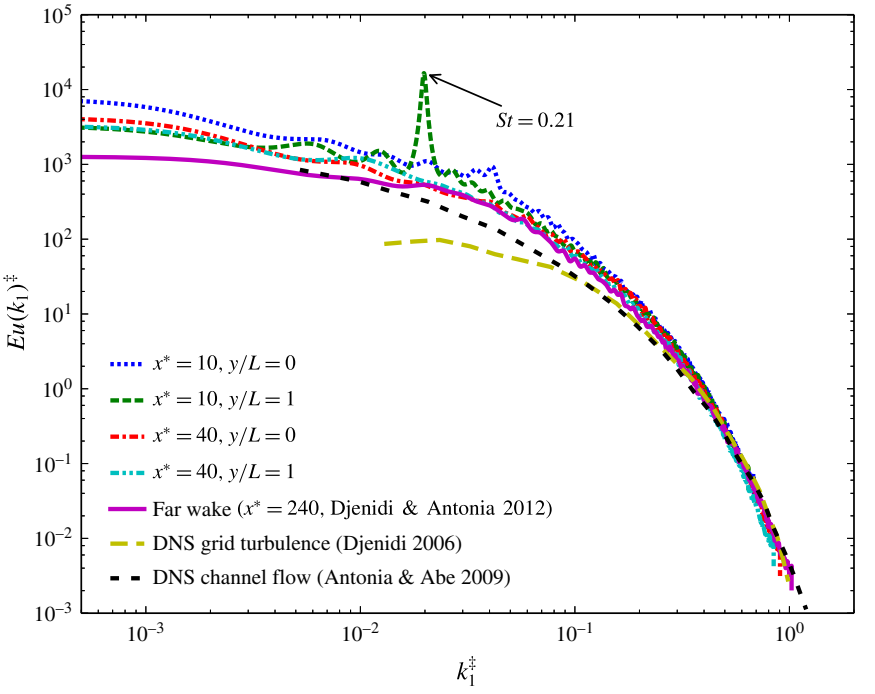

FIGURE 8. (Colour online) Longitudinal velocity spectra normalized by Kolmogorov scales, in which $\overline{\varepsilon}_{yz}$ is used, for $y/L = 0$ and $y/L = 1$ at $x^* = 10$ and 40, compared with those at the centreline of the far wake ($R_\lambda = 40$), and in DNS grid turbulence ($R_\lambda = 40$) and the centreline of the channel flow ($R_\lambda = 147$).

scales η and $u_K (\equiv (\nu\overline{\varepsilon})^{1/4})$. This has been verified through several compilations (e.g. Chapman 1979; Saddoughi & Veeravalli 1994). It should, however, be stressed that Antonia *et al.* (2014) pointed out that Kolmogorov's two main requirements, *viz.* very large Reynolds number and isotropic small-scale structures, can be relaxed, provided the effect of the large scales is negligible. This implies that the first similarity hypothesis may be satisfied in the present flow, where the coherent vortices are present and Re_λ is relatively small (table 1). Figure 8 shows that the spectrum of u scales on $\overline{\varepsilon}_{yz}$ and ν, both on the centreline ($y/L = 0$) and at the location where the shear is large ($y/L = 1$). Also included are spectra in the far wake at $x^* = 240$ (Djenidi & Antonia 2012), a turbulent grid flow (Djenidi 2006) and the centreline of channel flow (Antonia & Abe 2009). It shows that the velocity spectra at $x^* = 10$ and 40 in the present flow collapse reasonably well onto the other three normalized spectra in the literature which are in conformity with the universal spectrum over sufficiently high wavenumbers (say $k_1^{\ddagger} \approx 0.25$–$0.65$). The attenuation of the present spectra for $k_1^{\ddagger} > 0.65$ is due mainly to the imperfect spatial resolution of the probe (Zhu & Antonia 1996*c*; Zhou *et al.* 2003*a*).

The reasonable agreement between the velocity spectra of the present flow and those in the literature in the dissipation range bolsters the claim that the spectral chart method is robust, and implies that the application of the method to the present flow seems warranted. A comparison between the mean energy dissipation rate using the spectral chart method and estimates from (1.5), (1.10), (1.11), (1.12) at the centreline are shown in figure 9. The mean energy dissipation rate obtained with

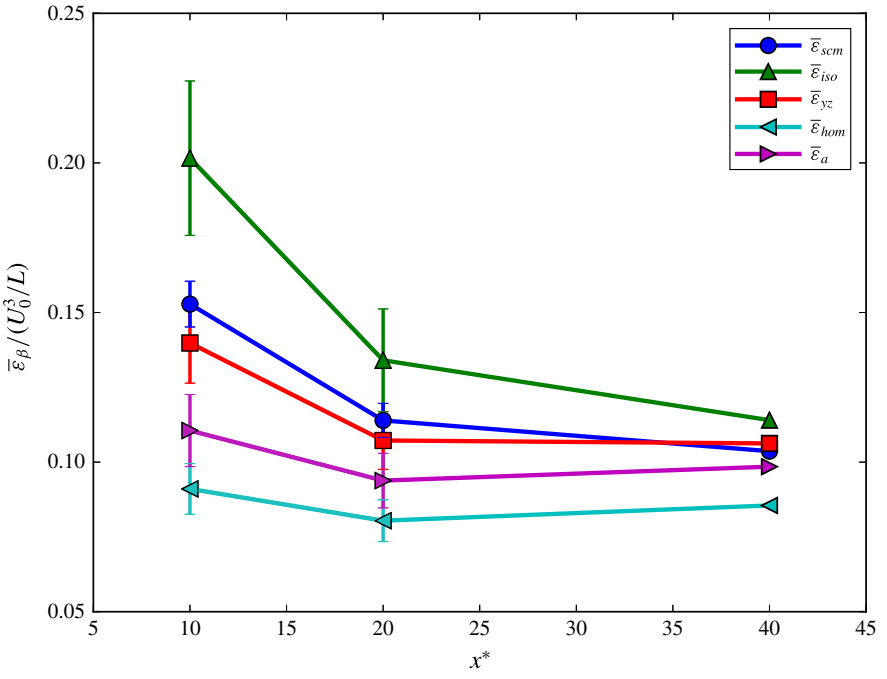

FIGURE 9. (Colour online) Comparison between different surrogates of $\overline{\varepsilon}$, i.e. $\overline{\varepsilon}_{iso}$ (1.5), $\overline{\varepsilon}_a$ (1.10), $\overline{\varepsilon}_{hom}$ (1.11), $\overline{\varepsilon}_{scm}$ estimated using the chart method, and the reference value $\overline{\varepsilon}_{yz}$ (1.12), on the wake centreline at $x^* = 10$, 20 and 40. Error bars for $x^* = 10$ and 20 are shown.

the spectral chart method, $\overline{\varepsilon}_{scm}$, is closer to the reference energy dissipation rate $\overline{\varepsilon}_{yz}$ than the other surrogates of (1.5), (1.10) and (1.11) at the same x^*. The differences between $\overline{\varepsilon}_{scm}$ and $\overline{\varepsilon}_{yz}$ are approximately 9.3 %, 6.3 %, 2.5 %, respectively, at $x^* = 10$, 20 and 40, which are satisfactorily small. The relatively larger difference at $x^* = 10$ is reasonable since the anisotropic large-scale motion is stronger there and the measurement attenuation is worse (table 1). Besides, we also have checked that $\overline{\varepsilon}_{yz}$ are 3.9 and 0.40 at $y/L = 1$ of $x/d = 10$ and 40, respectively, and the corresponding values based on the spectral chart method $\overline{\varepsilon}_{scm}$ are 3.4 and 0.36. The departures between $\overline{\varepsilon}_{scm}$ and $\overline{\varepsilon}_{yz}$ at $y/L = 1$ are 13 % and 10 % for $x/d = 10$ and 40, respectively. They are larger than the departures between $\overline{\varepsilon}_{scm}$ and $\overline{\varepsilon}_{yz}$ on the centreline (9.3 % and 2.5 % for $x/d = 10$ and 40, respectively). This should be due to the effect of the large shear at $y/L = 1$, which causes the flow to be locally more anisotropic than on the centreline. It is interesting to see that the isotropic estimation $\overline{\varepsilon}_{iso}$ always larger than $\overline{\varepsilon}_{yz}$ in the present flow, by 44 %, 25 % and 7 %, respectively, at $x^* = 10$, 20 and 40, which is in contrast to the far wake, where $\overline{\varepsilon}_{iso}$ always underestimates the total dissipation rate (e.g. Browne *et al.* 1987). The large difference between $\overline{\varepsilon}_{iso}$ and $\overline{\varepsilon}_{yz}$ at $x^* = 10$ and 20 is a reflection of the strong anisotropy there, as is also indicated by the evident scatter in the velocity derivative variances at $x^* = 10$ and 20 in figure 5(*a*,*b*). At $x^* = 40$, the smaller difference between $\overline{\varepsilon}_{iso}$ and $\overline{\varepsilon}_{yz}$ is consistent with the improved agreement among the velocity derivatives (figure 5*c*). The difference between the axisymmetric estimate of $\overline{\varepsilon}_a$ and $\overline{\varepsilon}_{yz}$ (21 %, 13 %, 7 %) is smaller than that between $\overline{\varepsilon}_{iso}$ and $\overline{\varepsilon}_{yz}$, which is consistent with the conclusion in

§ 4 that local axisymmetry is a better descriptor of the small-scale turbulent motions than local isotropy. The $\overline{\varepsilon}_{hom}$ always underestimates $\overline{\varepsilon}_{yz}$ and is the smallest of all the surrogates, which is partly due to the attenuation of the imperfect spatial resolution of the probe. Note that the different surrogates tend to converge towards $\overline{\varepsilon}_{yz}$ as the flow develops downstream and the influence of the coherent motions degrades.

The validity of the spectral chart method in a flow perturbed by coherent motions may seem somewhat surprising. Some additional remarks about the test of Kolmogorov's first similarity hypothesis seem worthwhile. Although the longitudinal velocity spectra are widely used in the literature to test the hypothesis (see Frisch 1996; Pope 2000), presumably because of the ease with which u is measured with a single hot wire, vorticity is more closely associated with small-scale turbulence than velocity (e.g. Antonia *et al.* 1996; Chen *et al.* 2017). Antonia *et al.* (1996) found that the shape of the high-wavenumber range of the vorticity spectrum, which appears to be independent of Re_λ, is also compatible with the first similarity hypothesis in the sense it scales uniquely on $\overline{\varepsilon}$ and ν. They also pointed out that the vorticity spectrum can provide a more sensitive test of the first similarity hypothesis than the velocity spectrum, since the major contribution to the vorticity variance is located at larger wavenumbers than for the velocity variance. The isotropic (also axisymmetric) form of the spectra of the vorticity fluctuations are given by Kim & Antonia (1993)

$$E_{\omega_x}(k_1) = \frac{1}{2}\int_{k_1}^{\infty} \frac{E(k)}{k}(k^2 - k_1^2)\,\mathrm{d}k, \tag{5.1}$$

$$E_{\omega_y}(k_1) = E_{w_z}(k_1)\frac{1}{2}k_1^2\int_{k_1}^{\infty} \frac{E(k)}{k}\,\mathrm{d}k + \frac{1}{4}\int_{k_1}^{\infty} \frac{E(k)}{k}(k^2 - k_1^2)\,\mathrm{d}k, \tag{5.2}$$

where $E(k)$ is the three-dimensional energy spectrum and k is the magnitude of the wavenumber vector $\boldsymbol{k}$. Figure 10 compares the normalized spectra of the three vorticity components on the centreline at $x^* = 10$ and 40 with the DNS spectra (Kim & Antonia 1993) of ω_x and ω_z on the channel flow centreline. At $x^* = 10$ (figure 10*a*), the spectrum of ω_z shows a pronounced peak at the wavenumber corresponding to $St = 0.21$, and deviates from the spectrum of ω_y. None of the three vorticity spectra collapse on the corresponding spectra of the channel flow at high wavenumbers. However, as the Kármán vortex impairs from $x^* = 10$ to 40 (figure 10*b*), the peak at $St = 0.21$ of $E_{\omega_z}(k_1)^{\ddagger}$ degrades and its high-wavenumber part collapses onto that of $E_{\omega_y}(k_1)^{\ddagger}$, and both $E_{\omega_z}(k_1)^{\ddagger}$ and $E_{\omega_y}(k_1)^{\ddagger}$ are in good agreement with the DNS spectrum of ω_z of the channel flow at high wavenumbers. There is also good agreement with the DNS spectrum of ω_x for the spectrum $E_{\omega_x}(k_1)^{\ddagger}$ at high wavenumbers. Again, the departures at high wavenumbers is ascribed to the inadequate spatial resolution of the probe, which is more evident than that of the velocity spectra (figure 8). The comparison between measured and DNS vorticity spectra at $x^* = 10$ and 40 suggests that the small-scale similarity is likely to be satisfied only at $x^* = 40$. This is contrary to the collapse of the velocity spectra both at $x^* = 10$ and 40 shown in figure 8, and supports Antonia *et al.*'s (1996) assertion that vorticity spectra provide a more sensitive test of the first similarity hypothesis than velocity spectra. It also confirms the expectation that large-scale coherent structures indeed have an effect on the small-scale motions at $x^* = 10$, whereas this effect is quite weak at $x^* = 40$.

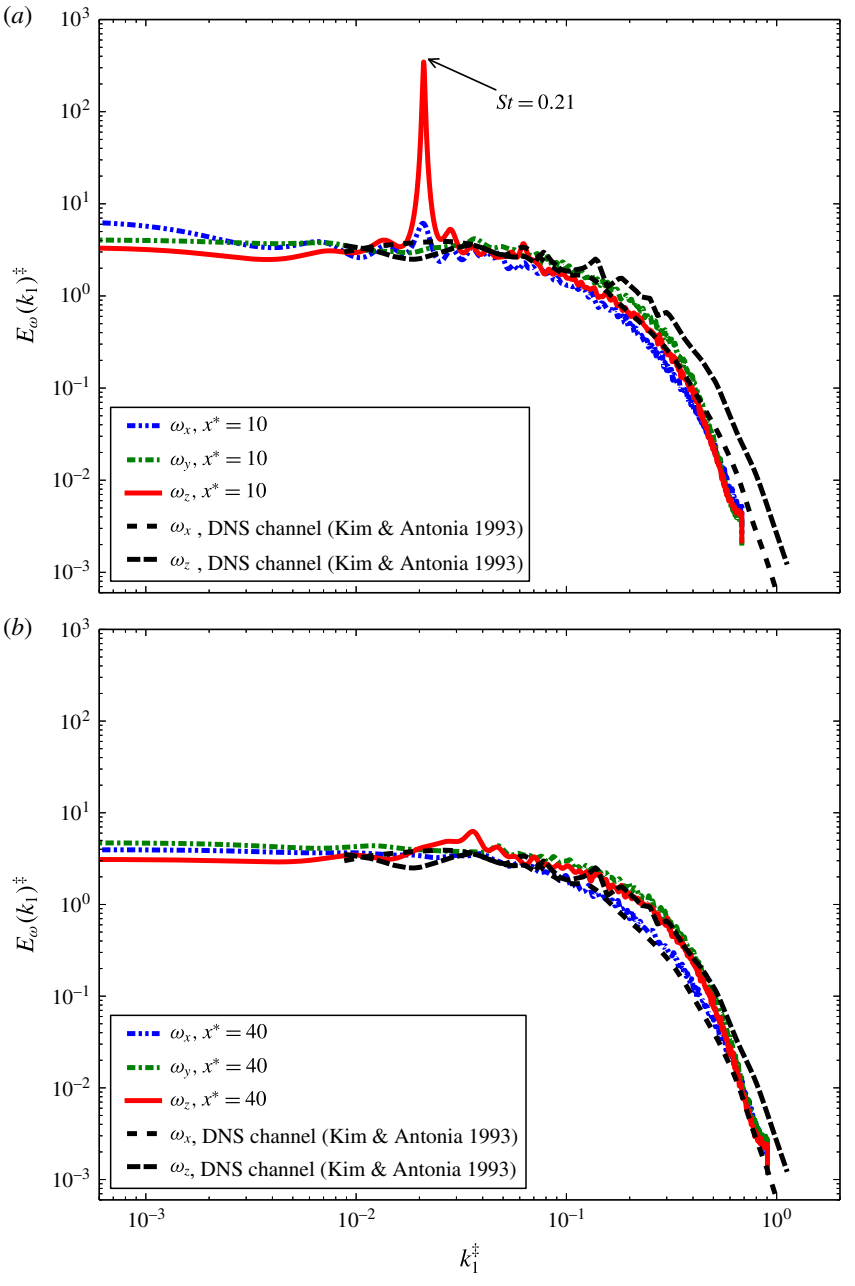

FIGURE 10. (Colour online) Comparison between the spectra of the three vorticity components of the present flow on the centreline at $x^* = 10$ and 40, and the spectra of ω_x and ω_z on the centreline of a DNS channel flow from Kim & Antonia (1993) ($R_\lambda = 53$). $\overline{\varepsilon}_{yz}$ is used in the normalization of the present vorticity spectra.

6. Phase-averaged energy dissipation rate and its components

A very distinct feature in the intermediate wake is the dominance of the Kármán vortex street at small x^*, which is followed by its gradual weakening and eventual

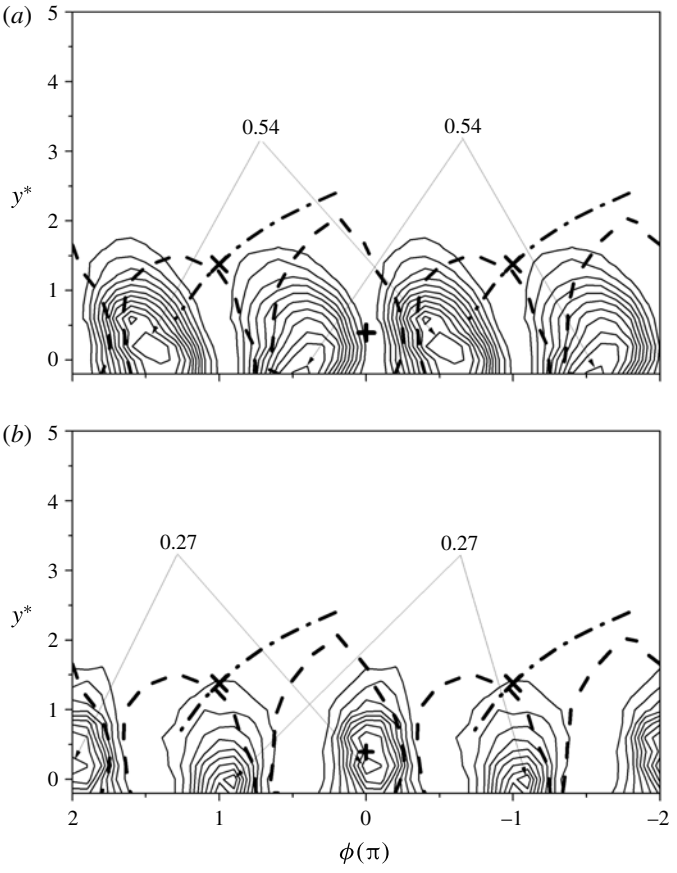

FIGURE 11. Isocontours of phase-averaged $\partial u/\partial y$ and $\partial v/\partial x$ variance at $x^* = 10$: (*a*) $(\widetilde{\partial u/\partial y}^*)^2$, contour interval = 0.049; (*b*) $(\widetilde{\partial v/\partial x}^*)^2$, contour interval = 0.030.

disappearance as x^* increases. It is thus of great interest to investigate the spatial distribution of the turbulent energy dissipation rate as the Kármán vortices evolve through their various stages. Hereinafter, the phase ϕ in the isocontour plot (figures 11–13) will be interpreted in terms of a longitudinal distance based on Taylor's hypothesis, $\phi = 0$–2π corresponding to the vortex wavelength. The same scale is used for the longitudinal and lateral directions in the contour plots in an effort to minimize any possible distortion in the physical space. The positions of the centres and saddle points, identified from the phase-averaged sectional streamlines (not shown), are marked by '+' and '×', respectively. The thick dashed lines give an approximate idea of the boundary of the spanwise vortex, which is approximately 25 % of the maximum value of $|\widetilde{\omega_z}|$ (not shown). The inclined dash-dotted line passing through the saddle point represents the diverging separatrix. The flow is left to right.

6.1. *Phase-averaged* $\partial u/\partial y$ *and* $\partial v/\partial x$

Figure 11 shows the phase-averaged isocontours of two components of the energy dissipation rate, $(\widetilde{\partial u/\partial y}^*)^2$ and $(\widetilde{\partial v/\partial x}^*)^2$, at $x^* = 10$, which have the maximum

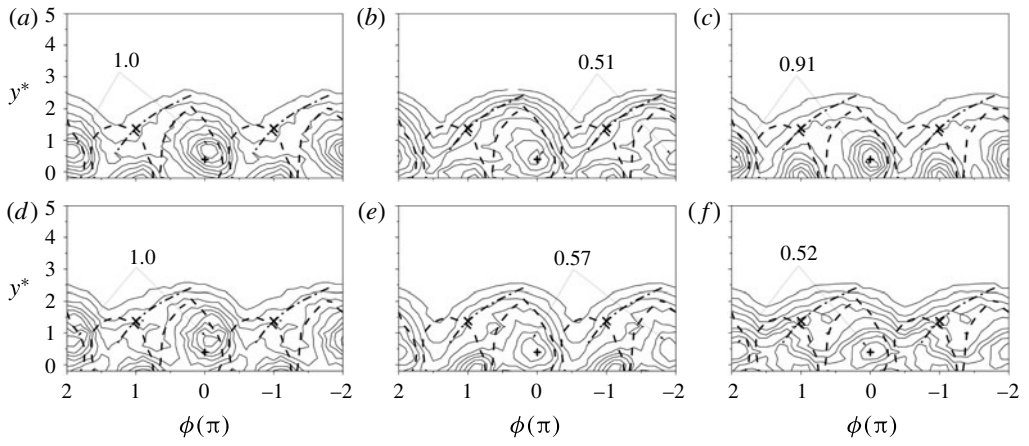

FIGURE 12. Isocontours of the remainders of the velocity derivatives at $x^* = 10$. (*a*) $\langle(\partial v/\partial x)_r^2\rangle^*$, contour interval: 0.11; (*b*) $\langle(\partial v/\partial z)_r^2\rangle^*$, contour interval: 0.057; (*c*) $\langle(\partial v/\partial y)_r^2\rangle^*$, contour interval: 0.10; (*d*) $\langle(\partial w/\partial x)_r^2\rangle^*$, contour interval: 0.11; (*e*) $\langle(\partial w/\partial y)_r^2\rangle^*$, contour interval: 0.081; (*f*) $\langle(\partial u/\partial z)_r^2\rangle^*$, contour interval: 0.058.

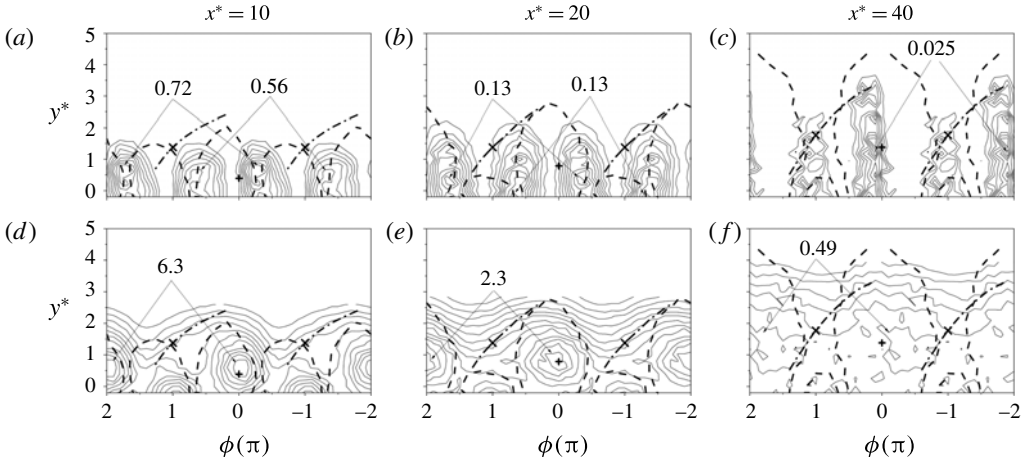

FIGURE 13. Phase-averaged turbulent energy dissipation rate (*a–c*) $\widetilde{\varepsilon}_{yz}^*$ and (*d–f*) the remainder $\langle\varepsilon_{yz,r}\rangle^*$: (*a*,*d*) $x^* = 10$, contour intervals: 0.080, 0.57; (*b*,*e*) 20, contour intervals: 0.015, 0.16; (*c*,*f*): 40, contour intervals: 0.0028, 0.072.

concentrations approximately one order of magnitude larger than those of the other measured velocity derivatives. This is mainly because $(\widetilde{\partial u/\partial y}^*)^2$ and $(\widetilde{\partial v/\partial x}^*)^2$ are associated with the coherent spanwise vorticity $\widetilde{\omega}_z^*(= \widetilde{\partial v/\partial x}^* - \widetilde{\partial u/\partial y}^*)$ which is the predominant coherent vorticity component. The larger maximum concentration of $(\widetilde{\partial u/\partial y}^*)^2$ and $(\widetilde{\partial v/\partial x}^*)^2$ is also internally consistent with the noticeable peak in the spectra of $\partial u/\partial y$ and $\partial v/\partial x$ at $St = 0.21$ shown in figure 7. The concentration of $(\widetilde{\partial u/\partial y}^*)^2$ occurs near the vortex boundary, while that of $(\widetilde{\partial v/\partial x}^*)^2$ coincides approximately with the vortex centre. There is a phase shift of approximately $\pi/2$

between the maximum concentrations of $(\widetilde{\partial u/\partial y}^*)^2$ and $(\widetilde{\partial v/\partial x}^*)^2$. The different behaviours of $(\widetilde{\partial u/\partial y}^*)^2$ and $(\widetilde{\partial v/\partial x}^*)^2$ reflect largely the distinct influence of the anisotropic large-scale motions on the velocity derivatives. Note that the maximum concentration of $(\widetilde{\partial u/\partial y}^*)^2$ is approximately 2 times that of $(\widetilde{\partial v/\partial x}^*)^2$, which is ascribed to the influence of the mean shear $\partial\overline{U}/\partial y$ since the large-scale strain of the mean shear can enhance the energy of the smallest scales (Thiesset *et al.* 2014).

While $(\widetilde{\partial u/\partial y}^*)^2$ and $(\widetilde{\partial v/\partial x}^*)^2$ play a dominant role among the coherent velocity derivatives, the situation is quite different for their remainders, which are associated with the remaining smaller-scale motions. Figure 12 shows the isocontours of the remainders of the six measured velocity derivatives at $x^* = 10$ which are involved in the axisymmetry equations (1.6*a–c*). In distinct contrast to the disparity in the topologies of the coherent velocity derivatives, the distributions of the remainders are comparable to each other, which is reasonable since the small-scale structures of the velocity derivatives are expected to be less anisotropic compared to the large-scale structures. Interestingly, the maximum concentrations of the remainders of the velocity derivatives are consistent with the local axisymmetry assumption. For instance, the maximum concentration of $\langle(\partial v/\partial x)_r^2\rangle^*$ (1.0, figure 12*a*) is equal to that of $\langle(\partial w/\partial x)_r^2\rangle^*$ (1.0, figure 12*d*); the maximum concentration of $\langle(\partial v/\partial z)_r^2\rangle^*$ (0.51, figure 12*b*) is approximately equal to that of $\langle(\partial w/\partial y)_r^2\rangle^*$ (0.57, figure 12*e*). Both conform to (1.6*b*,*c*). In contrast, there is a significant difference between their coherent isocontours. The different behaviours of the large and small scales of the velocity variances confirm our claim in § 4 that axisymmetry tends to be satisfied first in the small scales. Note that (1.6*a*) does not appear to be satisfied, as the maximum concentration of $\langle(\partial u/\partial y)_r^2\rangle^*$ (0.91, figure 12*c*) is larger than that of $\langle(\partial u/\partial z)_r^2\rangle^*$ (0.52, figure 12*f*). This is likely to be associated with the effect of the mean shear $\partial\overline{U}/\partial y$. The scenario is similar for the remainders at $x^* = 20$ and 40 (not shown), although the topologies gradually become less organized as x^* increases.

6.2. *Phase-averaged energy dissipation rate*

Figure 13 presents the isocontours of the phase-averaged energy dissipation rate and the remainder at all three x^* positions. The coherent energy dissipation rate (figure 13*a–c*) exhibits a distribution similar to that of $(\widetilde{\partial u/\partial y}^*)^2$ (figure 11*a*), which makes a dominant contribution to $\widetilde{\varepsilon}_{yz}^*$. Actually, the maximum percentage contribution of $(\widetilde{\partial u/\partial y}^*)^2$ to $\widetilde{\varepsilon}_{yz}^*$ can be as large as almost 80 % near the wake centreline at $x^* = 10$. On the other hand, the contribution of $(\widetilde{\partial v/\partial x}^*)^2$ to $\widetilde{\varepsilon}_{yz}^*$ near the vortex centre tends to be cancelled by the negative contribution from $2(\widetilde{\partial u/\partial y})^*(\widetilde{\partial v/\partial x})^*$ (not shown). The concentrations of the remainder $\langle\varepsilon_{yz,r}\rangle^*$ (figure 13*d–f*) coincide very well with the Kármán vortex, as the remainders of the velocity derivatives do (figure 12). We have also examined the phase-averaged and remainder isocontours (not shown) of the other three surrogates for the energy dissipation rate (1.5), (1.10) and (1.11). Their concentrations of the remainder are very similar to those of $\langle\varepsilon_{yz,r}\rangle^*$. The maximum concentrations of the coherent energy dissipation rate (figure 13*a–c*, 0.72, 0.13, 0.025 at $x^* = 10$, 20 and 40, respectively) are much smaller than those of the remainder (figure 13*d–f*, 6.3, 2.3, 0.49 at $x^* = 10$, 20 and 40, respectively) at the same x^*. This is not unexpected, since the energy dissipation occurs primarily at small scales (e.g. Pope 2000; Vassilicos 2015). It seems that the predominant

turbulent energy dissipation takes place within the Kármán vortices, at least for $x^* \leqslant 20$. The observation of the remainder energy dissipation rate is consistent with Hussain & Hayakawa's (1987) finding that the incoherent turbulence intensity occurs largely within the Kármán vortex at $x^* = 10$ to 40, and its maximum concentration almost coincides with the Kármán vortex centre. Since the turbulent energy dissipation rate physically reflects the rate at which the turbulent energy is dissipated into heat at small scales, its spatial distribution is expected to be associated with that of the remainder or the smaller-scale turbulent energy. At $x^* = 40$ (figure 13*c*,*f*), the Kármán vortices are quite weak due to vortex interactions and breakup. As a result, both the topologies of the coherent energy dissipation rate and the remainder appear markedly less organized. Nevertheless, the maximum concentration of the remainder remains discernible within the Kármán vortex boundary.

6.3. *Coherent contribution to the mean energy dissipation rate*

The isocontours of $(\widetilde{\partial u/\partial y}^*)^2$, $(\widetilde{\partial v/\partial x}^*)^2$ (figure 11) and $\widetilde{\varepsilon}^*_{yz}$ (figure 13) show very well organized structures at $x^* = 10$ which are apparently correlated with the Kármán vortices. Further, the maximum concentration of $(\widetilde{\partial u/\partial y}^*)^2$ and $(\widetilde{\partial v/\partial x}^*)^2$ can be comparable to that of $\langle(\partial u/\partial y)_r^2\rangle^*$ and $\langle(\partial v/\partial x)_r^2\rangle^*$, whereas the concentration of the coherent part of the other velocity derivatives (not shown) is quite small compared to their remainders. The results suggest that the coherent motions make a much larger contribution to $\overline{(\partial u/\partial y)^2}$ and $\overline{(\partial v/\partial x)^2}$ than to the other velocity derivative terms, which intrinsically reflects the way the small scales feel the influence from the large scales associated with the Kármán vortices. The coherent contribution from the coherent motions at a given y^* position can be quantified by the ratio of the structural average of the phase-averaged coherent quantity to the corresponding Reynolds-averaged quantity (Zhou *et al.* 2003*b*), namely

$$\alpha = \overline{\widetilde{\beta}\widetilde{\gamma}}/\overline{\beta\gamma}, \tag{6.1}$$

where β and γ represent the velocity derivatives $\partial u_i/\partial x_j$ as those in §§ 3.1 and 3.2. Figure 14 presents the distribution of α of $\overline{(\partial u/\partial y)^2}$ and $\overline{(\partial v/\partial x)^2}$ and $\overline{\varepsilon}_{yz}$ across the wake at the three x^* positions. The coherent contribution to the mean energy dissipation rate, i.e. $\overline{\widetilde{\varepsilon}}_{yz}/\overline{\varepsilon}_{yz}$, is calculated, where $\overline{\widetilde{\varepsilon}}_{yz}$ is estimated as the sum of the structural average of all the terms on the right-hand side of (1.12). At $x^* = 10$ (figure 14*a*), the coherent contribution accounts for up to 35 % of $\overline{(\partial u/\partial y)^2}$ and 18 % of $\overline{(\partial v/\partial x)^2}$, respectively, near the centreline. Such large coherent contributions are consistent with the pronounced peak at $St = 0.21$ in the spectra of $\partial u/\partial y$ and $\partial v/\partial x$ (figure 7*a*), as well as the organized structures displayed by $(\widetilde{\partial u/\partial y}^*)^2$ and $(\widetilde{\partial v/\partial x}^*)^2$ (figure 11). The maximum coherent contribution to $\overline{\varepsilon}_{yz}$ is approximately 9 % at $y^* = 0.6$ which corresponds roughly to the lateral location of the maximum concentration of $\widetilde{\varepsilon}^*_{yz}$. The relatively small coherent contribution to $\overline{\varepsilon}_{yz}$, compared with that to $\overline{(\partial u/\partial y)^2}$ and $\overline{(\partial v/\partial x)^2}$, reflects the very small coherent contributions to the other components of $\overline{\varepsilon}_{yz}$. The distinct difference between the coherent contribution to $\overline{(\partial u/\partial y)^2}$ and $\overline{(\partial v/\partial x)^2}$ and those to the other velocity derivative terms reflects that the small scales feel the influence from the large scales associated with the Kármán vortices mainly via $\partial u/\partial y$ and $\partial v/\partial x$. The effect of the large-scale motions can still

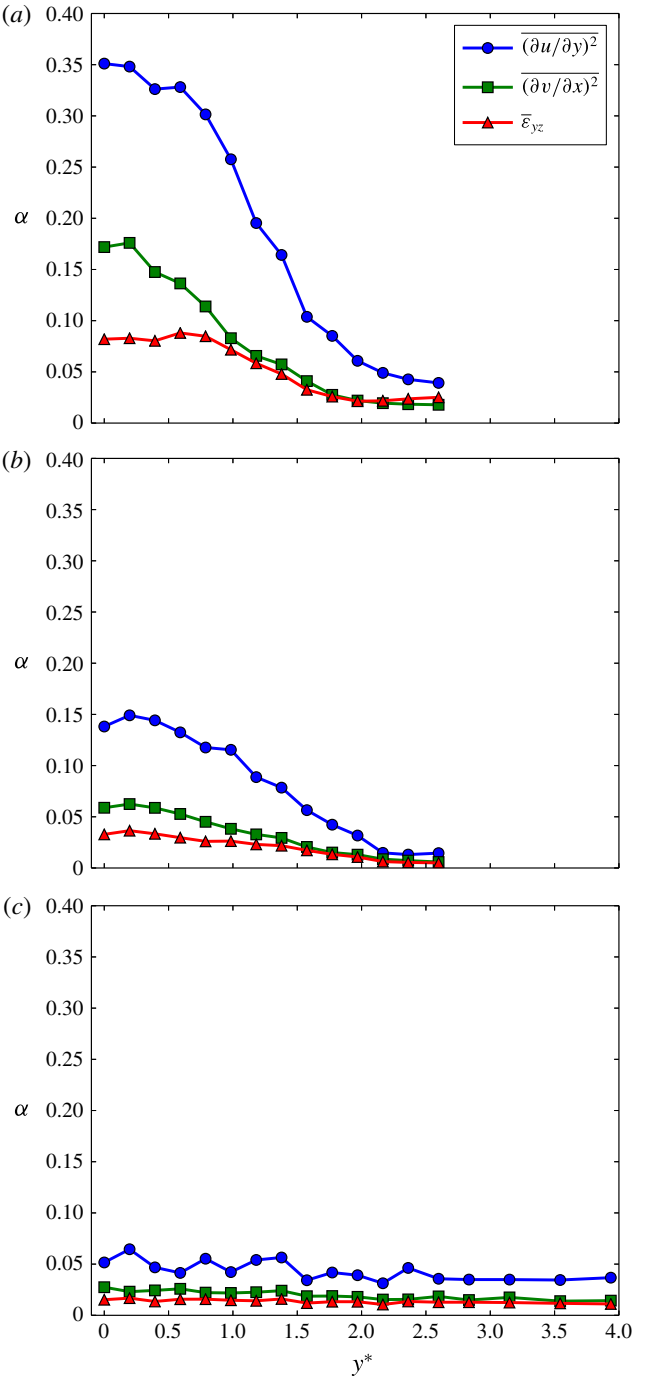

FIGURE 14. (Colour online) Coherent contributions (α) to $\overline{(\partial u/\partial y)^2}$, $\overline{(\partial v/\partial x)^2}$, and $\overline{\varepsilon}_{yz}$ across the wake at (*a*) $x^* = 10$; (*b*) 20 and (*c*) 40.

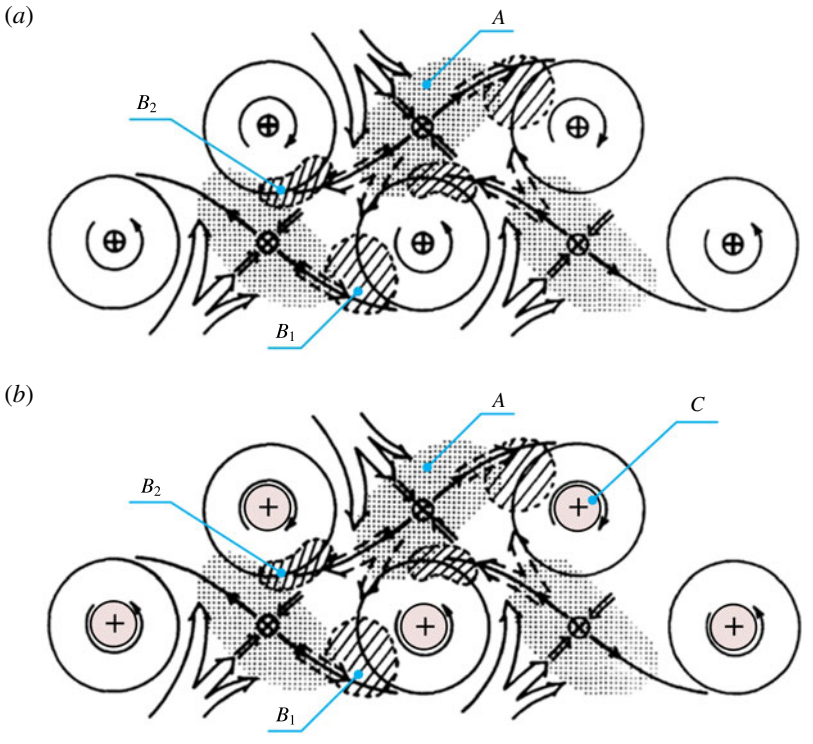

FIGURE 15. (Colour online) (*a*) Hussain and Hayakawa's original topological model and (*b*) the modified model of the flow in a plane wake (+, vortex centre; ×, saddle point; ⇒ engulfed non-turbulent fluid; ==> flow of produced turbulence; *A*: turbulence production; B_1 and B_2: turbulent mixing; *C*: turbulent kinetic energy dissipation).

be felt at $x^* = 20$ (figure 14*b*), where the maximum coherent contributions to $\overline{(\partial u/\partial y)^2}$, $\overline{(\partial v/\partial x)^2}$ and $\overline{\varepsilon}_{yz}$ are approximately 15 %, 6 % and 4 %, respectively. Because of the rather weak coherent motions at $x^* = 40$, the coherent contribution there is negligibly small (figure 14*c*).

6.4. *Topological model of the flow*

In his review on coherent structures in turbulence, Hussain (1986) surmised that the ribs can induce spanwise contortions of rollers and cause mixing and dissipation, mostly at locations where they connect with rollers. A topological model (figure 15*a*) was proposed in Hussain & Hayakawa (1987) to explain the mechanism of the turbulent plane wake. Since the energy dissipation rate was not measured by these authors, the model did not contain any information on the spatial distribution of the energy dissipation rate. Figure 13 shows unequivocally that the predominant turbulent energy dissipation rate, i.e. $\langle \varepsilon_{yz,r} \rangle^*$, is mostly concentrated within the spanwise vortex, particularly when the Kármán vortex is strong ($x^* = 10$ and 20). The spatial distribution of the energy dissipation rate within the Kármán vortex is consistent with the observations from DNS of homogeneous turbulence (e.g. Kerr 1985; Rogers & Moin 1987; She, Jackson & Orszag 1990) that intense vorticity regions occur in vortex tubes and the energy dissipation rate is strongly correlated with these tubes. Actually, a strong correlation between large values of the enstrophy and the large

energy dissipation rates has also been found in the turbulent far wake (e.g. Zhu & Antonia 1996*a*).

Based on the present spatial distribution of the energy dissipation rate, a more complete picture emerges for the turbulence dynamics by incorporating the information on the energy dissipation rate into Hussain & Hayakawa's model, as shown in figure 15(*b*). In the revised model, the saddle region (denoted as A), where intense strain is induced by the rotating motion of successive vortices, can be identified with the turbulent energy production area. The non-turbulent fluid from the free stream is engulfed into the rotating motion of the ribs (or quasi-streamwise vortices) and is subjected to the strain associated with vortex stretching along the diverging separatrix, leading to the production of turbulence. Turbulent mixing should occur mostly in the region (denoted as B_1 and B_2) where the streamwise vortex and the spanwise vortex are in contact with each other (Hussain & Hayakawa 1987). Chen *et al.* (2016) found that the interaction between the ribs and von Kármán vortices takes place mostly near the centreline at small x^* positions (say $x^* = 10$), causing the distortion of the rollers and enhancing the turbulent mixing. The turbulence produced in the saddle region is entrained by the rotational motion of the spanwise vortex and accumulated within the vortex structure (denoted as C) before being finally dissipated further downstream.

It should be noted that, although the present experiment is conducted with a moderate Reynolds number, the topological feature of the energy dissipation rate is believed to be applicable in larger Reynolds numbers. This expectation is supported by the fact that the flow structures in the wake of a circular cylinder are essentially unchanged as long as Re is less than its critical value, approximately 2.5×10^5 (Zdravkovich 1997). As a matter of fact, Yiu *et al.* (2004) studied the Re effect on the three-dimensional vorticity in a turbulent cylinder wake ($x^* = 10$–40) with $Re = 2500$, 5000 and 10 000, and demonstrated that the topology of the wake is similar for these Reynolds numbers, although the three-dimensionality of the flow is enhanced at higher Re.

7. Summary and conclusions

Ten of the twelve terms which make up the mean energy dissipation rate are measured simultaneously with a four X-wire probe at three streamwise locations in a turbulent intermediate wake. Both the statistical and the topological features of the energy dissipation rate as well as its components are examined. Four major conclusions can be drawn from this study.

(1) Local axisymmetry is a better descriptor of the small-scale turbulent motions than local isotropy. The mean square velocity derivative terms satisfy local axisymmetry better than local isotropy. Neither local isotropy nor local axisymmetry are satisfied by the correlation terms. Spectra of velocity derivatives indicate that axisymmetry is first satisfied at high wavenumbers; the departure at low wavenumbers is related to the effect of the Kármán vortices. This effect gradually weakens between $x^* = 10$ and $x^* = 40$, so that the low-wavenumber part of the spectra begins to satisfy axisymmetry.

(2) The close agreement between $\overline{\varepsilon}_{yz}$ and $\overline{\varepsilon}_{scm}$ estimated via the spectral chart method proposed by Djenidi & Antonia (2012) indicates that this method, which is based on the collapse, over the dissipative range, of the longitudinal velocity spectrum normalized by Kolmogorov scales, is also applicable for the present flow. $\overline{\varepsilon}_{scm}$ is closer to $\overline{\varepsilon}_{yz}$ than the other three surrogates ($\overline{\varepsilon}_{iso}$, $\overline{\varepsilon}_{a}$, $\overline{\varepsilon}_{hom}$) at the same x^*. It is found that despite the effect of the anisotropic large-scale coherent motions and mean shear at $x^* = 10$, the dissipative range of the u spectra collapses onto the

reference universal spectra in previous studies (figure 8), while the high-wavenumber part of the normalized vorticity spectra only starts to comply with isotropy at $x^* = 40$. It confirms Antonia *et al.*'s (2014) observation that the two major assumptions in Kolmogorov's first similarity hypothesis can be relaxed in the context of the collapse of the spectrum of u in the dissipative range; it also confirms that the vorticity spectrum is a more sensitive test of this hypothesis than the velocity spectrum.

(3) Both $\partial u/\partial y$ and $\partial v/\partial x$ play a crucial role in the interaction between large- and small-scale motions in this flow. These velocity derivatives contain mainly information on the small-scale motion since the bulk of their variances is located at high wavenumbers (figure 7). The maximum coherent contribution associated with Kármán vortices to $\overline{(\partial u/\partial y)^2}$ and $\overline{(\partial v/\partial x)^2}$ can be as high as 35 % and 18 %, respectively, near the wake centreline at $x^* = 10$. This is largely because $\partial u/\partial y$ and $\partial v/\partial x$ are associated with the most organized vorticity component $\omega_z (= \partial v/\partial x - \partial u/\partial y)$. On the other hand, the coherent contributions to the other velocity derivative variances are almost one order of magnitude smaller than those to $\overline{(\partial u/\partial y)^2}$ and $\overline{(\partial v/\partial x)^2}$, leading to a quite small coherent contribution (maximum value being approximately 9 % at $x^* = 10$) to the total mean energy dissipation rate. Thiesset *et al.* (2014) found that, close to the wake generator ($x^* = 10$), the influence of the coherent motions can be felt by even the smallest scales. This study further indicates that the coherent motions in the present flow interact with the small-scale turbulent structures mostly via $\partial u/\partial y$ and $\partial v/\partial x$.

(4) Isocontours of the phase-averaged energy dissipation rate $\widetilde{\varepsilon}_{yz}$ are quite similar to those of $\widetilde{(\partial u/\partial y)^2}$, which is the major contributor to $\widetilde{\varepsilon}_{yz}$. The concentrations of the remainder $\langle \varepsilon_{yz,r} \rangle$, whose maximum is nearly one order of magnitude larger than that of the coherent concentrations of $\widetilde{\varepsilon}_{yz}$ (figure 13), occur mainly within the Kármán vortices. The same observation applies to the remainder of the other energy dissipation rate surrogates ($\langle \varepsilon_{iso,r} \rangle$, $\langle \varepsilon_{a,r} \rangle$, $\langle \varepsilon_{hom,r} \rangle$). It is therefore concluded that the dominant energy dissipation mainly takes place within the Kármán vortex. A more complete picture for the flow mechanism is proposed by incorporating this information into Hussain & Hayakawa's (1987) model. In the new model, turbulence is produced in the saddle region and is then transported into the vortex structures aligned with the diverging separatrix before being finally dissipated within the Kármán vortex.

Acknowledgements

Y.Z. wishes to acknowledge support given to him from NSFC through grant 11632006. The support from the Chinese Scholarship Council to J.G.C. is also acknowledged.

REFERENCES

ABE, H., ANTONIA, R. A. & KAWAMURA, H. 2009 Correlation between small-scale velocity and scalar fluctuations in a turbulent channel flow. *J. Fluid Mech.* **627**, 1–32.

ANTONIA, R., ORLANDI, P. & ZHOU, T. 2002 Assessment of a three-component vorticity probe in decaying turbulence. *Exp. Fluids* **33**, 384–390.

ANTONIA, R. A. & ABE, H. 2009 Inertial range similarity for velocity and scalar spectra in a turbulent channel flow. In *Proceedings of the Sixth International Symposium on Turbulence, Heat and Mass Transfer, Rome, Italy*, Begell House.

ANTONIA, R. A., ANSELMET, F. & CHAMBERS, A. J. 1986 Assessment of local isotropy using measurements in a turbulent plane jet. *J. Fluid Mech.* **163**, 365–391.

ANTONIA, R. A., DJENIDI, L. & DANAILA, L. 2014 Collapse of the turbulent dissipative range on Kolmogorov scales. *Phys. Fluids* **26**, 45105.

ANTONIA, R. A., KIM, J. & BROWNE, L. 1991 Some characteristics of small-scale turbulence in a turbulent duct flow. *J. Fluid Mech.* **233**, 369–388.

ANTONIA, R. A. & MI, J. 1998 Approach towards self-preservation of turbulent cylinder and screen wakes. *Exp. Therm. Fluid Sci.* **17**, 277–284.

ANTONIA, R. A., SHAFI, H. S. & ZHU, Y. 1996 A note on the vorticity spectrum. *Phys. Fluids* **8**, 2196–2202.

ANTONIA, R. A., SHAH, D. A. & BROWNE, L. W. B. 1988 Dissipation and vorticity spectra in a turbulent wake. *Phys. Fluids* **31**, 1805–1807.

ANTONIA, R. A., ZHU, Y. & KIM, J. 1993 On the measurement of lateral velocity derivatives in turbulent flows. *Exp. Fluids* **15**, 65–69.

BROWNE, L., ANTONIA, R. A. & SHAH, D. A. 1987 Turbulent energy dissipation in a wake. *J. Fluid Mech.* **179**, 307–326.

CHAPMAN, D. R. 1979 Computational aerodynamics development and outlook. *AIAA J.* **17**, 1293–1313.

CHEN, J. G., ZHOU, T. M., ANTONIA, R. A. & ZHOU, Y. 2017 Comparison between passive scalar and velocity fields in a turbulent cylinder wake. *J. Fluid Mech.* **813**, 667–694.

CHEN, J. G., ZHOU, Y., ZHOU, T. M. & ANTONIA, R. A. 2016 Three-dimensional vorticity, momentum and heat transport in a turbulent cylinder wake. *J. Fluid Mech.* **809**, 135–167.

DJENIDI, L. 2006 Lattice-Boltzmann simulation of grid-generated turbulence. *J. Fluid Mech.* **552**, 13.

DJENIDI, L. & ANTONIA, R. A. 2009 Momentum and heat transport in a three-dimensional transitional wake of a heated square cylinder. *J. Fluid Mech.* **640**, 109–129.

DJENIDI, L. & ANTONIA, R. A. 2012 A spectral chart method for estimating the mean turbulent kinetic energy dissipation rate. *Exp. Fluids* **53**, 1005–1013.

FRISCH, U. 1996 *Turbulence: The Legacy of A. N. Kolmogorov*. Cambridge University Press.

GEORGE, W. & HUSSEIN, H. 1991 Locally axisymmetric turbulence. *J. Fluid Mech.* **233**, 1–23.

GULITSKI, G., KHOLMYANSKY, M., KINZELBACH, W., LÜTHI, B., TSINOBER, A. & YORISH, S. 2007 Velocity and temperature derivatives in high-Reynolds-number turbulent flows in the atmospheric surface layer. Part 1. Facilities, methods and some general results. *J. Fluid Mech.* **589**, 57–81.

HUANG, J. F., ZHOU, Y. & ZHOU, T. 2006 Three-dimensional wake structure measurement using a modified PIV technique. *Exp. Fluids* **40**, 884–896.

HUSSAIN, A. 1986 Coherent structures and turbulence. *J. Fluid Mech.* **173**, 303–356.

HUSSAIN, A. K. M. F. 1983 Coherent structures – reality and myth. *Phys. Fluids* **26**, 2816–2850.

HUSSAIN, A. K. M. F. & HAYAKAWA, M. 1987 Eduction of large-scale organized structures in a turbulent plane wake. *J. Fluid Mech.* **180**, 193–229.

HUSSEIN, H. J. 1994 Evidence of local axisymmetry in the small scales of a turbulent planar jet. *Phys. Fluids* **6**, 2058–2070.

KERR, R. M. 1985 Higher-order derivative correlations and the alignment of small-scale structures in isotropic numerical turbulence. *J. Fluid Mech.* **153**, 31–58.

KIM, J. & ANTONIA, R. A. 1993 Isotropy of the small scales of turbulence at low Reynolds number. *J. Fluid Mech.* **251**, 219–238.

KOLMOGOROV, A. N. 1941 The local structure of turbulence in incompressible viscous fluid for very large Reynolds numbers. *Dokl. Akad. Nauk SSSR* **30**, 301–305.

LANDAU, L. D. & LIFSCHITZ, E. M. 1987 *Fluid Mechanics*. Butterworth Heinemann.

LEFEUVRE, N., THIESSET, F., DJENIDI, L. & ANTONIA, R. A. 2014 Statistics of the turbulent kinetic energy dissipation rate and its surrogates in a square cylinder wake flow. *Phys. Fluids* **26**, 95104.

MI, J. & ANTONIA, R. A. 2010 Approach to local axisymmetry in a turbulent cylinder wake. *Exp. Fluids* **48**, 933–947.

MOHAMED, M. S. & LARUE, J. C. 1990 The decay power law in grid-generated turbulence. *J. Fluid Mech.* **219**, 195–214.

POPE, S. B. 2000 *Turbulent Flows*. Cambridge University Press.

ROGERS, M. M. & MOIN, P. 1987 Helicity fluctuations in incompressible turbulent flows. *Phys. Fluids* **30**, 2662–2671.

SAARENRINNE, P. & PIIRTO, M. 2000 Turbulent kinetic energy dissipation rate estimation from PIV velocity vector fields. *Exp. Fluids* **29**, S300–S307.

SADDOUGHI, S. G. & VEERAVALLI, S. V. 1994 Local isotropy in turbulent boundary layers at high Reynolds number. *J. Fluid Mech.* **268**, 333–372.

SHAFI, H. S. & ANTONIA, R. A. 1997 Small-scale characteristics of a turbulent boundary layer over a rough wall. *J. Fluid Mech.* **342**, 263–293.

SHE, Z.-S., CHEN, S., DOOLEN, G., KRAICHNAN, R. H. & ORSZAG, S. A. 1993 Reynolds number dependence of isotropic Navier–Stokes turbulence. *Phys. Rev. Lett.* **70**, 3251–3254.

SHE, Z.-S., JACKSON, E. & ORSZAG, S. A. 1990 Intermittent vortex structures in homogeneous isotropic turbulence. *Nature* **344**, 226–228.

SREENIVASAN, K. R. & ANTONIA, R. A. 1997 The phenomenology of small-scale turbulence. *Annu. Rev. Fluid Mech.* **29**, 435–472.

TANG, S. L., ANTONIA, R. A., DJENIDI, L. & ZHOU, Y. 2015 Transport equation for the isotropic turbulent energy dissipation rate in the far-wake of a circular cylinder. *J. Fluid Mech.* **784**, 109–129.

TAYLOR, G. I. 1935 Statistical theory of turbulence. *Proc. R. Soc. Lond.* A **151**, 421–444.

TENNEKES, H. & LUMLEY, J. L. 1972 *A First Course in Turbulence*. MIT Press.

THIESSET, F., DANAILA, L. & ANTONIA, R. A. 2013 Dynamical effect of the total strain induced by the coherent motion on local isotropy in a wake. *J. Fluid Mech.* **720**, 393–423.

THIESSET, F., DANAILA, L. & ANTONIA, R. A. 2014 Dynamical interactions between the coherent motion and small scales in a cylinder wake. *J. Fluid Mech.* **749**, 201–226.

VASSILICOS, J. C. 2015 Dissipation in turbulent flows. *Annu. Rev. Fluid Mech.* **47**, 95–114.

WALLACE, J. M. 2009 Twenty years of experimental and direct numerical simulation access to the velocity gradient tensor: what have we learned about turbulence? *Phys. Fluids* **21**, 21301.

WALLACE, J. M. & FOSS, J. F. 1995 The measurement of vorticity in turbulent flows. *Annu. Rev. Fluid Mech.* **27**, 469–514.

YIU, M. W., ZHOU, Y., ZHOU, T. & CHENG, L. 2004 Reynolds number effects on three-dimensional vorticity in a turbulent wake. *AIAA J.* **42**, 1009–1016.

ZDRAVKOVICH, M. M. 1997 *Flow Around Circular Cylinders*. Oxford University Press.

ZHOU, T. & ANTONIA, R. A. 1992 Convection velocity measurements in a cylinder wake. *Exp. Fluids* **13**, 63–70.

ZHOU, T. & ANTONIA, R. A. 2000 Reynolds number dependence of the small-scale structure of grid turbulence. *J. Fluid Mech.* **406**, 81–107.

ZHOU, T., ANTONIA, R. A., LASSERRE, J. J., COANTIC, M. & ANSELMET, F. 2003*a* Transverse velocity and temperature derivative measurements in grid turbulence. *Exp. Fluids* **34**, 449–459.

ZHOU, T., PEARSON, B. R. & ANTONIA, R. A. 2001 Comparison between temporal and spatial transverse velocity increments in a turbulent plane jet. *Fluid Dyn. Res.* **28**, 127–138.

ZHOU, T., RAZALI, S. M., ZHOU, Y., CHUA, L. P. & CHENG, L. 2009 Dependence of the wake on inclination of a stationary cylinder. *Exp. Fluids* **46**, 1125–1138.

ZHOU, T., ZHOU, Y., YIU, M. W. & CHUA, L. P. 2003*b* Three-dimensional vorticity in a turbulent cylinder wake. *Exp. Fluids* **35**, 459–471.

ZHOU, Y. & ANTONIA, R. A. 1995 Memory effects in a turbulent plane wake. *Exp. Fluids* **19**, 112–120.

ZHU, Y. & ANTONIA, R. A. 1996*a* On the correlation between enstrophy and energy dissipation rate in a turbulent wake. *Appl. Sci. Res.* **57**, 337–347.

ZHU, Y. & ANTONIA, R. A. 1996*b* Spatial resolution of a 4-X-wire vorticity probe. *Meas. Sci. Technol.* **7**, 1492–1497.

ZHU, Y. & ANTONIA, R. A. 1996*c* The spatial resolution of hot-wire arrays for the measurement of small-scale turbulence. *Meas. Sci. Technol.* **7**, 1349–1359.